Contributions to Mineralogy and Petrology (2022) 177:96
https://doi.org/10.1007/s00410-022-01962-1

ORIGINAL PAPER

Inferences on the magmatic plumbing system at Stromboli volcano (Italy) from trace element geochemistry of matrix glasses and minerals in different types of explosive eruptions

Patrizia Landi[1] · Claudia D'Oriano[1] · Maurizio Petrelli[2] · Manuela Nazzari[3] · Daniele Andronico[4]

Received: 18 January 2022 / Accepted: 15 September 2022

Abstract

Stromboli (Italy) is a basaltic volcano characterized by persistent, mild strombolian activity, occasionally interrupted by lava effusion and more violent explosive events, named major explosions and paroxysms depending on their intensity and magnitude. The normal activity is fed by a shallow and degassed highly porphyritic (HP) shoshonitic basalt carrying about 50 vol.% crystals settled in a shoshonitic glassy matrix ($K_2O > 3.8$ wt.%). The more energetic explosions erupt a deep, volatile-rich, low-porphyritic (LP) magma with < 10 vol.% crystals in a shoshonitic basaltic glassy matrix ($K_2O < 2.4$ wt.%). Products with intermediate glass composition are also found in the more violent explosive events. In this study, we present a new data set of major and trace element contents in matrix glasses and minerals performed in products from different types of explosive activity that occurred at Stromboli between 1998 and 2020. This large data set is used to put constraints on the evolution and architecture of the intermediate plumbing system, where the transformation from LP to HP occurs. Results indicate that, compared to paroxysms, the glassy matrices of the LP pumices from major explosions are richer in incompatible trace elements (and K_2O wt.%) due to < 15 wt.% fractionation of clinopyroxene and olivine. This points to a chemical zoning of the deep reservoir and suggests that major explosions are fed by magmas residing in its upper part. Among the major explosions, the homogeneous intermediate glasses in the products from the 19 July 2020 event originate from the interplay of mixing and crystal fractionation processes. The crystallization of euhedral microphenocrysts of An-rich plagioclase suggests that batches of magma can pond and crystallize for few days (< 11) at the base of the intermediate zone of the plumbing system, at pressure coinciding with the entering of plagioclase into the system (< 100 MPa). As a relevant point for understanding the pre- and syn-eruptive magma dynamics, data indicate a positive correlation between the magnitude of the explosions and the depth of the supply magma.

Keywords Stromboli explosive activity · Matrix glass · Trace elements · Petrogenetic processes

Introduction

Stromboli island (Aeolian Archipelago, South Italy) is a steady-state volcano characterized by persistent activity since the eighth century CE (Rosi et al. 2013). The eruptive activity takes place from several vents located within a flat crater area at about 750 m a.s.l. in the upper part of the Sciara del Fuoco, a horseshoe-shaped scar in the NW flank of the island generated by several flank collapses (Tibaldi et al. 2001). The "normal" activity of the volcano consists of continuous degassing accompanied by rhythmic, mild to moderate explosions from a single vent, lasting from a few to tens of seconds, which throw ash, lapilli, and bombs up to heights of several hundreds of meters (Harris and Ripepe 2007; Rosi et al. 2013). This is occasionally interrupted by lava effusion

Communicated by Gordon Moore.

✉ Claudia D'Oriano
claudia.doriano@ingv.it

[1] Istituto Nazionale di Geofisica e Vulcanologia, Sezione di Pisa, via Cesare Battisti 53, 56127 Pisa, Italy

[2] Dipartimento di Fisica e Geologia, Piazza dell'Università, Università degli Studi di Perugia, 06123 Perugia, Italy

[3] Istituto Nazionale di Geofisica e Vulcanologia, Sezione di Roma1, Via Di Vigna Murata 605, 00143 Rome, Italy

[4] Istituto Nazionale di Geofisica e Vulcanologia, Osservatorio Etneo, Sezione di Catania, Piazza Roma 2, 95125 Catania, Italy

Published online: 29 September 2022

episodes and more violent explosive events during which several vents can be involved and ejection velocity and volume of products are much higher than during normal explosions. The more violent explosive events (named paroxysms by Mercalli et al. 1907) are short-lived explosions (from tens of seconds to a few minutes) classified as "major explosions" or "paroxysms," depending on the areal distribution of the products and hazard implications, intensity and magnitude of the eruption, the paroxysms being the most energetic events (Barberi et al. 1993; Harris and Ripepe 2007; Bertagnini et al. 2008; Rosi et al. 2013). Some authors (i.e., Métrich et al. 2021) further distinguished the paroxysms between "small-scale paroxysms" (e.g., 5 April 2003; 15 March 2007; 3 July 2019; 28 August 2019) and "large-scale paroxysms" (e.g., 1930 and 1456 CE eruptions). Each explosion of the normal activity is characterized by a tephra volume of 1–10 m^3 and a Mass Discharge Rate of 10^2–10^3 kg/s; major explosions typically erupt 10^2–10^3 m^3 of tephra with a Mass Discharge Rate of 10^4–10^5 kg/s, while, during paroxysms, the volume of the erupted products reaches 10^4–10^5 m^3 with Mass Discharge Rate of 10^6–10^7 kg/s (Rosi et al. 2013 and references therein; Andronico et al. 2021).

Extensive literature, focused on the characterization of geochemical and petrological features of the magmas emitted at Stromboli, reveals that the normal activity is fed by a crystal-rich basaltic-shoshonitic magma, with a shoshonitic matrix glass ($K_2O \geq 3.8$ wt.%), hosting about 50 vol.% of crystals (HP magma = Highly Porphyritic), including oscillatory-zoned plagioclase ($An_{60–90}$), clinopyroxene (Mg# 0.70–0.90; $Fs_{5–17}$) and fairly homogeneous olivine ($Fo_{70–74}$). Rims of plagioclase and pyroxene in textural equilibrium with the HP matrix glasses have composition ~ $An_{62–70}$ (peaked at An_{68}) and Mg#0.73–0.78 ($Fs_{12–14}$), respectively. Minerals are commonly euhedral, although in a few cases they display rounded rims with compositions out of equilibrium with the groundmass glasses (Landi et al. 2004, 2009; Francalanci et al. 2004; Bertagnini et al. 2008). This magma resides in a degassed shallow reservoir (< 3 km), located within the volcanic edifice. The shallow magma body maintains its nearly stationary conditions through a continuous supply of a volatile-rich, low-porphyritic (LP) magma ascending from the deeper portions of the plumbing system, down at 6–9 km. LP magma has a basaltic-shoshonitic matrix glass ($K_2O \leq 1.7$–2.4 wt.%), and < 10 vol.% of clinopyroxene ($Mg\#_{0.84–0.90}$; $Fs_{5–8}$) and olivine $Fo_{82–91}$ (Métrich et al. 2001, 2010, 2021; Francalanci et al. 2004; Landi et al. 2004, 2009; Armienti et al. 2007; Bertagnini et al. 2008). In detail, olivine compositions $Fo_{88–91}$ as reverse zoned or composite crystals are peculiar in the products from the large-scale paroxysms and are indicative of a deep recharge (depth > 9 km) accompanying these powerful explosions (Bertagnini et al. 2003, 2008; Métrich et al. 2021). Plagioclases in LP products are only found as reaction/growth rims on phenocrysts mostly inherited from the HP magma, or aggregates of skeletal microlites, with variable composition around An_{70}–An_{88} (Landi et al. 2004; Andronico et al. 2021). At shallow levels, the LP magma degasses, crystallizes, and mixes with the resident magma, generating the HP magma (Métrich et al. 2001; Landi et al. 2004).

The products with intermediate composition between LP and HP melts show a strongly inhomogeneous glassy matrix that covers the entire range between the two end-members (Andronico et al. 2008; Andronico and Pistolesi 2010; La Felice and Landi 2011a; Pioli et al. 2014). Mineral compositions in equilibrium with these intermediate glasses are until now not documented as phenocrysts, and they can be only found as reaction/growth rims that commonly develop on crystals inherited from the LP or HP magmas (Landi et al. 2008; La Felice and Landi 2011a), making difficult the identification of a distinctive mineral paragenesis.

Magmas with intermediate characteristics are thought to originate from hybridization and mineral dissolution/crystallization during HP/LP magma mixing and degassing, likely within a strongly dynamic, intermediate zone of the feeding system between 1 and 4 km (Francalanci et al. 2004, 2012; Métrich et al. 2010; Landi et al. 2008; La Felice and Landi 2011a; Pioli et al. 2014). However, a physical and chemical model of this zone is up to date not available.

Although during normal activity a small amount of deep-derived LP magma (< 3 vol.%) detected in the ash fraction can reach the surface (Schiavi et al. 2010; D'Oriano et al. 2011), paroxysms and most of the major explosions involve relevant volumes of LP magma that mingles with the shallow HP magma during its ascent. The extent of mingling is largely variable among the clasts of a single explosion and among clasts from different paroxysms/major explosions (Bertagnini et al. 2008; Rosi et al. 2013; Andronico et al. 2021; Métrich et al. 2021). In some major explosions, emitted products are characterized by only HP composition (e.g., 8 September 1998; Bertagnini et al. 1999), while other major events are characterized by the emission of both HP and LP magmas, associated with a variable quantity of products with intermediate composition between the two end-members. All the different compositions can be found in a single clast (mingled pumice). Among the previously studied eruptions characterized by the emission of intermediate compositions, the LP end-member is absent only in the products from the 9 January 2005 explosion, a high-energy event ranking between major explosions and normal activity (Andronico et al. 2008; Pioli et al. 2014).

In this work, we present trace element analyses of the glassy matrices and mineral phases of volcanic products that erupted during different types of explosive activity at Stromboli over a period of 22 years. We use this large data set to discuss the role of the different petrogenetic processes (degassing, crystallization, mineral dissolution, magma

mixing) that occur in the feeding system and lead to the transformation of the LP magma into the HP magma. The aim of the work is to improve the knowledge of the structure and evolution of the volcanic plumbing system with emphasis on the intermediate zone between the deep LP reservoir and the shallow HP magma body. Also, we provide insights into the relationships between the type of explosive activity at Stromboli volcano and the involved sectors of the plumbing system.

Studied samples

Studied samples are representative of the whole spectrum of explosive activity that occurred at Stromboli between 1998 and 2020, and correspond to 4 paroxysms, 8 major explosions, and 7 scoriae and/or ash emitted during the normal activity. Samples consist of: (1) mingled pumices sampled in the summit area of the volcano a few days after the more violent explosive events (both major explosions and paroxysms); (2) ash and lapilli emitted during the paroxysms and sampled along the coast or close to the villages of Ginostra and Stromboli; (3) HP scoriae emitted during the whole range of eruption intensity, from paroxysms to major explosions to normal activity; and (4) coarse ash emitted during the normal activity (Table 1; Online Resource 1).

Among the analyzed samples, those emitted before September 2019 were already object of petrographic, mineralogical and compositional studies. In detail, they are: the 5 April 2003 (Métrich et al. 2005), the 15 March 2007 (Métrich et al. 2010), and both the 2019 (Andronico et al. 2021) paroxysms; the 23 August 1998, 8 September 1998, 24 November 1998, 26 August 1999 (Bertagnini et al. 1999 and 2003; Métrich et al. 2001; Landi et al. 2004), and both the November 2009 (La Felice and Landi 2011a) major explosions; and the 18 July 2000 scoriae (ST212; Landi et al. 2004), the ash emitted in October 2011 (EST1; D'Oriano et al. 2011), the 27 July 2019 lapilli and ash (samples 17 and 22c, respectively; Andronico et al. 2021) emitted during normal activity.

Thanks to the effort gained in the frame of the UNO-Project, aimed at the characterization of the ordinary activity to predict the extraordinary, an intensification of the sampling at Stromboli allowed the collection of several samples in the period October 2019–October 2020. They correspond to the normal activity in October 2019 (STRO#1), November 2019 (STRO#8), and October 2020 (ST1020#5), and the products erupted during the major explosion of 19 July 2020. This last can be considered one of the most energetic major explosions that occurred at Stromboli in the past decades (Aiuppa et al., 2021). A survey following this episode allowed us to document that the explosion was characterized by the ejection of large scoria bombs in the summit area

Table 1 List of studied samples with indication of the type of activity in terms of explosion intensity (see text for details), the date of the event and the typology of material (LP = low porphyritic; HP = highly porphyritic; INT = intermediate)

Sample	Date	Type of activity	Material analyzed	Groundmass
ST137/ST130	23 August 1998	Major explosion	Mingled pumice	LP, HP
ST155	8 September 1998	Major explosion	Scoriae	HP
ST168	24 November 1998	Major explosion	Mingled pumice	LP, INT, HP
ST178	26 August 1999	Major explosion	Mingled pumice	LP, HP
ST212	18 July 2000	Normal activity	Scoriae	HP
ST305	5 April 2003	Paroxysm	Mingled pumice	LP, HP
15/03/07	15 March 2007	Paroxysm	Mingled pumice	LP, HP
EST1	October 2008	Normal activity	Coarse ash	HP
STR081109	8 November 2009	Major explosion	Mingled pumice	INT, HP
STRO241109	24 November 2009	Major explosion	Mingled pumice	LP, INT, HP
P02	3 July 2019	Paroxysm	Total sample (coarse ash)	LP, INT, HP
703a	3 July 2019	Paroxysm	Mingled pumice	LP, INT, HP
15	3 July 2019	Paroxysm	Scoriae	HP
17	end of July 2019	Normal activity	Lapilli	HP
22c	end of July 2019	Normal activity	Ash	HP
19c	28 August 2019	Paroxysm	Total sample (coarse ash)	LP, INT, HP
STRO#8	20 October 2019	Normal activity	Coarse ash	LP, HP
STRO#1	1 November 2019	Normal activity	Coarse ash	HP
STPL801	19 July 2020	Major explosion	Scoria coated by yellowish glass	INT, HP
STPL804	19 July 2020	Major explosion	Scoria coated by yellowish glass	INT, HP
STPL805	19 July 2020	Major explosion	Single scoria	HP
ST1020#5	10 October 2020	Normal activity	Coarse ash	HP

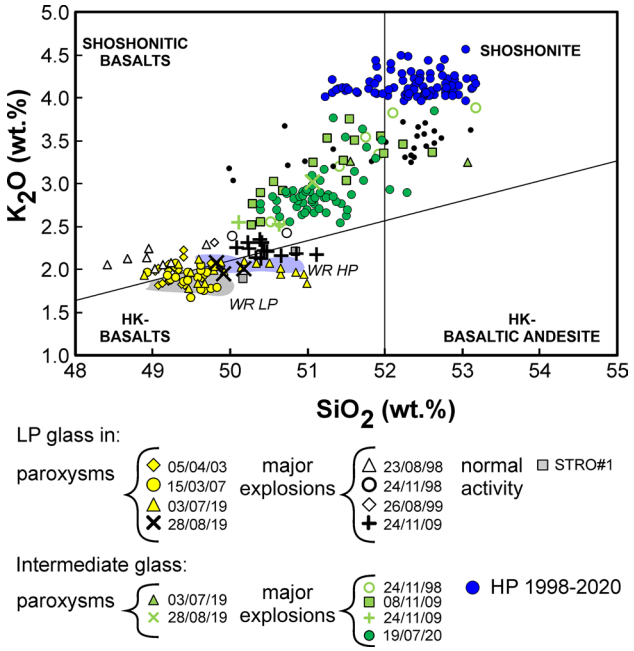

Fig. 1 Glass composition of the explosive products erupted in the period 1998–2020 plotted in the SiO_2 vs K_2O classification diagram (Peccerillo and Taylor 1976). The whole rock (WR) compositions from Métrich et al. (2001, 2005), Bertagnini et al. (2003), Landi et al. (2004, 2009) are reported for comparison as fields of variation (LP: gray; HP: blue). Black dots: 9 January 2005, data from Landi et al. (2009)

down to 700–750 m in the SW-SE sector, while on the E flank of the edifice the products were concentrated in a rather narrow lobe-shaped area down to 600 m a.s.l. The products deposited on the summit area mainly consist of black HP scoria bombs, partially coated by a highly vesicular, yellowish glass (Fig. 1a, b), while, on the E flank, homogeneous, dense HP scoriae are found. In both deposits, a reddish lithic material, mostly made of altered rocks ripped from the upper conduit and vent area, is abundant both as dm-sized blocks and mm-sized fragments within the scoria bombs. LP pumices were also erupted during this explosion (Bertagnini and Pistolesi personal communication) and likely dispersed from the plume as lapilli in the N–NE sector of the volcano. During our sampling, carried out three months after the major explosion, the LP material erupted during this event was no longer recognizable, due to its intrinsic crumbly character.

For the purpose of the present work, all samples reported in Table 1 were analyzed for their major and trace element glass composition. In addition, the 19 July 2020 samples were investigated for the petrographic and mineralogical features; major and trace element analyses of selected mineral phases were measured in samples ST130 (23 August 1998), ST305 (5 April 2005), and 15 (3 July 2019), and STPL804 (19 July 2020). See Online Resource1 for details on analyzed samples.

Methods

Textural characterization of groundmasses and phenocrysts, and major element composition of mineral phases were investigated at the Istituto Nazionale di Geofisica e Vulcanologia (INGV), Pisa (Italy) by means of a Zeiss EVO MA 10 scanning electron microscope (SEM) working in backscattered electron (BSE) mode, equipped with an Oxford ISIS microanalytical EDS system. The accuracy of EDS analyses is < 3–4% for most of the major elements and < 5% for Na_2O. Major element compositions of minerals selected for trace element analyses were also obtained by means of a Jeol-JXA8200 microprobe at INGV, Rome (see below).

Trace element composition of few plagioclase (11 spot analyses), pyroxenes (8 spot analyses) and olivines (16 spot analyses) and about 300 spot analyses of microlite-free matrix glasses were performed at the Dipartimento di Fisica e Geologia, University of Perugia (Italy) by laser ablation–inductively coupled plasma–mass spectrometry (LA-ICP-MS). The instrumentation consisted of a Teledyne Photon Machine G2 laser ablation device coupled to a Thermo Fisher Scientific iCAP Q quadrupole mass spectrometer (Petrelli et al. 2016a). Circular laser beams ranging from 20 to 40 µm, a repetition rate of 8 Hz, and a laser fluence of ~ 3.5 Jcm^{-1} have been utilized. Ablation times were about 30 s per spot, preceded by a 25 s background measurement and followed by 25 s of washout. Data reduction was completed with the Iolite 3 software (Paton et al. 2011). The NIST SRM 610 (Pearce et al. 1997) glass and the USGS BCR2G (Wilson 1997) reference materials were used as calibrator and quality control, respectively. The CaO concentrations obtained by electron microprobe were used as internal standard for the glass, plagioclase, and pyroxene, whereas SiO_2 was used for the olivine. Under the reported analytical conditions, the precision is better than 11% for concentrations above 0.1 ppm and better than 5% above 20 ppm; the accuracy is always better than 10% with the only exception of Sc, i.e., 12% (Online Resource 1, Petrelli et al. 2016a, b).

In addition, we included in the data set also LA-ICP-MS unpublished analyses of glass (60 spots) and minerals (39 spots), performed at the IGG-CNR of Pavia and the University of Cagliari, in 2001 and 2008, respectively. Precision (< 6%) and accuracy (< 14%) of the LA-ICP-MS analyses performed at Pavia are reported in Online Resource 1; for other details, refer to Landi et al. (2008). For details of LA-ICP-MS analyses performed at Cagliari, refer to D'Oriano et al. (2008).

Major element analyses close to LA spots were performed by means of a Jeol-JXA8200 combined EDS-WDS (five spectrometers with twelve crystals). Data

were collected using 15 kV accelerating voltage and 7.5 nA beam current. The beam diameter was 5 µm with a counting time of 10 and 5 s on peaks and background, respectively. The following internal international standards (MAC LTD) were used: orthoclase (Si, Al, K and Na), apatite (P and Ca), olivine (Mg), pyrite (Fe), rutile (Ti), and rhodonite (Mn). Sodium and potassium were analyzed first to prevent alkali migration effects. The precision and the accuracy of the microprobe were measured through repeated analyses of well-characterized synthetic oxide and mineral secondary standards. Based on counting statistics and analytical uncertainties relative to their reported concentrations, precision for major elements was better than 3% and accuracy better than 2%, except for Na in obsidian 6% (Online Resource 1).

Results

The matrix glasses of the products analyzed in the present study show a large textural and compositional variability (SiO_2 49–53 wt.%; Fig. 1), in agreement with what was observed in the previous works. The HP products have a scoriaceous appearance and their groundmasses are characterized by the presence of large bubbles, often irregularly shaped due to the effect of coalescence. In contrast, the LP products are yellow pumiceous material, texturally identified at SEM-BSE for the presence of many and small rounded vesicles, a microlite-free groundmass and the absence of euhedral plagioclase phenocrysts. Despite these textural differences, HP and LP magmas have a very similar whole rock composition (high potassium (HK) to shoshonitic basalts; Fig. 2), which, therefore, it is not suitable for investigating the petrogenetic processes that occur in the intermediate zone of the feeding system, while numerous information can be obtained from the textural and compositional analyses of the matrix glasses. In addition, LP/HP mingling is peculiar to the pumice clasts and whole rock of "pure" unmingled pumice is basically impossible to obtain. Products with intermediate compositions between the two end-members are generally associated with micron-scale spaced mingling textures, always detected straddling the LP and HP portions. Instead, the yellowish material which partially covers a part of the scoria bombs emitted in the 19 July 2020 major explosion (Fig. 2a, b) is characterized by nearly homogenous glasses with intermediate composition which appear as completely hybridized areas, and the contact between the intermediate and HP portions of the clasts is not shaded (Fig. 2c, d). In these products, the intermediate glasses are characterized by a vesicularity similar to that of LP pumices, even if some vesicles appear collapsed. Few microlites of plagioclase with swallowtail edges rapidly grew in the groundmass due to quenching of the less evolved, hotter intermediate magma at the contact with the cooler HP ones. The rheological (i.e., the changes in viscosity due to differences in temperature) differences between the pure HP and "intermediate" glass in the products from 19

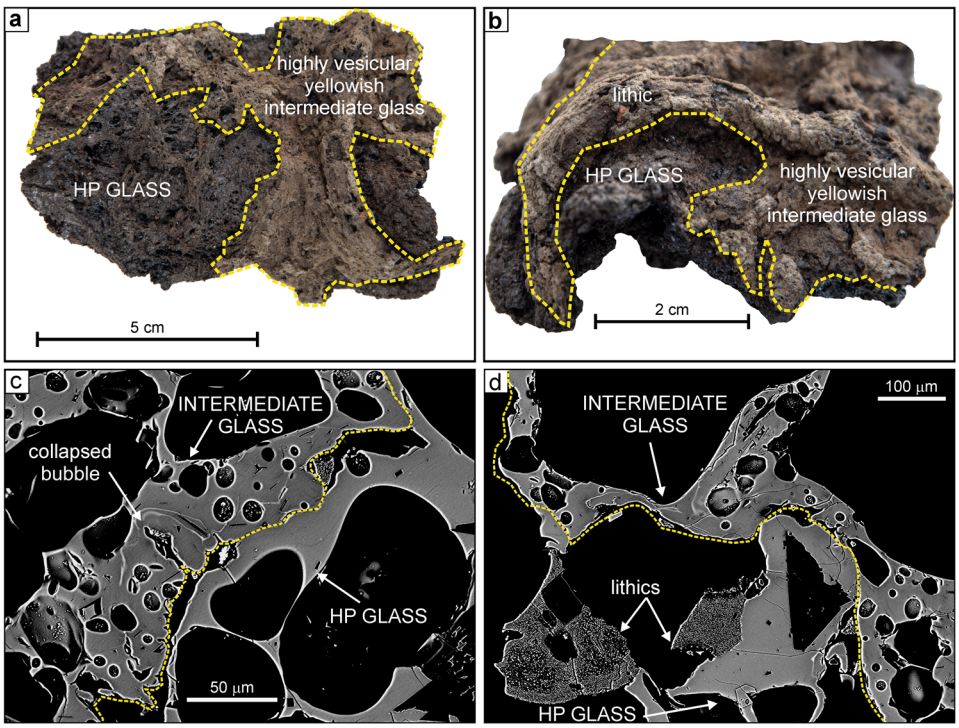

Fig. 2 Scoria bomb emitted during the major explosion on 19 July 2020. **a**, **b** The pictures show the macroscopic feature of the highly vesicular, yellowish material adhering on the external portion of the HP scoria bomb. **c**, **d** BSE-SEM images showing the contact between highly vesicular intermediate and HP glasses (sample STPL801_7b). The boundary of the intermediate zones develops a curling morphology (**c**); the contact is characterized by the presence of abundant lithic grains (**d**). In all images, the contact between intermediate and HP portions is marked by a yellow dashed line

July 2020 are also highlighted by the curling margins of the intermediate zones and by the presence of lithic ash clasts (Fig. 2c, d).

Mineral chemistry of the products from the 19 July 2020 major explosion

The HP products erupted during the major explosion of 19 July 2020 have the same petrographic characteristics observed in HP products erupted during the normal strombolian activity (Métrich et al. 2001; Francalanci et al. 2004; Landi et al. 2004). The mineral assemblage consists of euhedral crystals of zoned plagioclase, zoned clinopyroxene, and almost homogeneous olivine, hosted in a homogeneous shoshonitic glassy matrix (K_2O 4.0–4.2 wt.%). The rims of phenocrysts in textural equilibrium with the matrix glasses have a nearly homogeneous composition, characterized by plagioclase (pl) $An_{63–68}$, clinopyroxene (cpx) Mg# 0.74–0.77 ($Fs_{13–14}$) and olivine (ol) $Fo_{71–72}$ (Fig. 3a–c) (Table 2). Only a few phenocrysts of olivine with rounded shapes have Mg-rich rims up to $Fo_{74–75}$. Compositions $Fo_{74–75}$ are also found as thin rims (10–20 µm) in the rare olivine microlites (crystals < 100 µm).

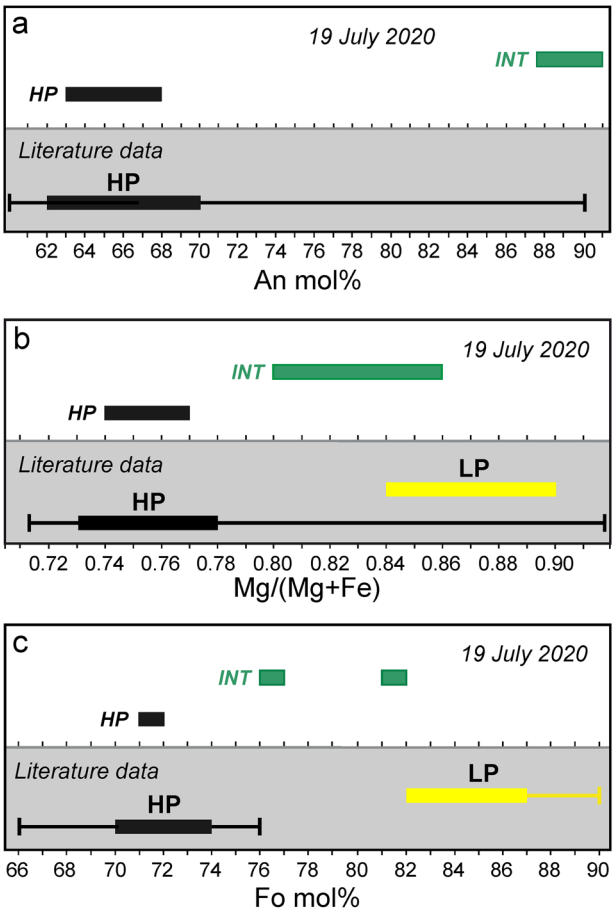

Fig. 3 Composition of the rims of (**a**) plagioclase (An mol.%), (**b**) clinopyroxene (Mg/(Mg + Fe)) and (**c**) olivine (Fo mol.%) in the products of the 19 July 2020 explosion. Black lines: rims of crystals in the HP products; green lines: rims of crystals wetted by intermediate glass. For comparison, the composition of the phenocrysts in HP and LP products taken from the literature are reported in the lower part of the diagrams; the thick lines represent the mineral compositions that are considered in equilibrium with the HP (black) and LP (yellow) melts (Bertagnini et al. 2003, 2008; Landi et al. 2009; Métrich et al. 2021)

The highly vesicular material adhering to the external portion of the HP scoria bombs is characterized by a low crystal content and a rather inhomogeneous mineral chemistry due to the occurrence of crystals with reaction rims inherited from both the HP and LP magmas (Table 2). Mafic minerals (cpx and ol) wetted by the intermediate glass with intermediate composition (K_2O 2.5–3.2 wt.%) are commonly found as crystal aggregates sometimes associated with plagioclase, while plagioclase is mostly present as single crystals. Pyroxenes have rounded and quite homogeneous cores (Mg# 0.69–0.73; $Fs_{15–19}$) mantled by nearly homogeneous rims, with composition from Mg# 0.82 to Mg# 0.86 (Fs_8–Fs_{10}) (Figs. 3a, 4a, b). The mantles can develop sector zoning (Fig. 4a). Large crystals of pyroxene (~ Fs_{14}; Mg# 0.75) wetted by the highly vesicular glass (K_2O 2.6–3.2 wt.%), develop thin rims, ~ 10–15 µm thick, with Mg# 0.80–0.82 ($Fs_{10–11}$). Olivine crystals found in aggregates are characterized by rounded cores ($Fo_{70–73}$) that progressively pass to less evolved rims with Fo_{76} to Fo_{82} (Fig. 3b, 4b). Plagioclase phenocrysts with dissolved labradoritic to bytownitic cores (inherited by HP magma; Landi et al. 2004) and encircled by a sieved texture An-rich (~ $An_{80–85}$) corona are commonly found (Fig. 4c). It is worthy of noting that the vesicular material is characterized by the occurrence of plagioclase with texture and composition never described in the products of Stromboli. These are microphenocrysts, 200–400 µm large, with An-rich ($An_{75–91}$) patchy zoned cores, hosting large vesicles and melt inclusions, that are encircled by undisturbed layers, up to 150 µm large, with homogeneous composition ($An_{87–91}$) (Fig. 4d–f). This type of crystals can be also found in aggregates with pyroxenes Mg# 0.82–0.86 (Fig. 4a). All plagioclase crystals have external rims < 10 µm ~ $An_{65–69}$, showing swallowtail final edges.

Major and trace element content in matrix glasses

Major and trace element compositions obtained on the whole spectrum of eruption intensity show that minor differences occur among the products related to each eruption in terms of: (1) variation fields of both LP and HP melts; and (2) occurrence and variability of intermediate terms. The K_2O content in the matrix glasses is used to distinguish among the LP (K_2O < 2.4 wt.%), the "intermediate" (K_2O 2.4–3.8 wt.%) and the HP (K_2O > 3.8 wt.%) melts. Although the concentration of some elements (i.e., both major oxides and

Table 2 Average major and trace element composition of matrix glasses, olivine, clinopyroxene and plagioclase representative of LP, intermediate and HP products

	Matrix glass				Olivine		Clinopyroxene				Plagioclase	
	Average 3 July 2019 ($n=22$)	Average 23 August 1998 (n = 10)	Average 19 July 2020 (n = 20)	Average sample 17 ($n=13$)	Average ST130-ST305	STPL804b-spot7	STPL804A-113	ST212-PX2-2	Average STPL801 7b (spot86-89)	STPL804A-112	Average STPL801 7b (spot 94–95.104–105.108)	ST212 (Pl7 rim)
	LP (pumice from paroxysm)	LP (pumice from major explosion)	Intermediate (yellow material on scoriae)	HP (scoria)	Ol Fo_{86}	$OlFo_{82.6}$	Cpx (Mg#0.91)	Cpx (Mg#0.87)	Cpx (Mg#0.85)	Cpx (Mg#0.75)	pl An_{90}	pl An_{67}
Major elements (wt.%)												
SiO_2	49.95 (0.67)	49.16 (0.43)	51.07 (0.40)	52.26 (0.37)	40.15 (0.40)	39.47	52.99	52.85	51.83 (0.25)	49.69 (0.31)	45.20 (0.28)	51.22 (0.21)
TiO_2	0.94 (0.07)	1.12 (0.08)	1.24 (0.10)	1.64 (0.10)			0.20	0.36	0.45 (0.05)	0.87 (0.04)		
Al_2O_3	17.79 (0.15)	17.49 (0.21)	17.43 (0.35)	15.95 (0.10)			1.84	2.05	3.02 (0.23)	4.93 (0.42)	35.45 (0.37)	30.64 (0.24)
FeO	8.04 (0.19)	8.34 (0.18)	8.87 (0.40)	10.09 (0.13)	13.57 (0.19)	16.5	3.01	4.66	5.34 (0.09)	7.17 (0.18)	0.58 (0.07)	0.73 (0.02)
MnO	0.12 (0.03)	0.15 (0.03)	0.12 (0.04)	0.15 (0.03)	0.18 (0.031)	0.31	0.04	0.15	0.15 (0.04)	0.19 (0.01)		
MgO	6.08 (0.12)	5.98 (0.17)	4.95 (0.26)	3.76 (0.08)	46.12 (0.40)	43.88	17.49	17.08	16.70 (0.20)	13.60 (0.44)		
CaO	11.11 (0.19)	11.07 (0.13)	9.22 (0.37)	7.40 (0.12)	0.25 (0.027)	0.26	23.23	22.19	21.97 (0.42)	20.38 (0.53)	18.51 (0.17)	13.57 (0.08)
Na_2O	2.53 (0.11)	2.85 (0.11)	2.97 (0.23)	3.28 (0.11)	bdl	bdl	0.15	0.28	0.14 (0.03)	0.63 (0.09)	1.07 (0.04)	3.22 (0.07)
K_2O	1.98 (0.09)	2.13 (0.08)	2.79 (0.23)	3.95 (0.08)	bdl	bdl	n.d	bdl		bdl		
P_2O_5	0.56 (0.09)	0.70 (0.49)	0.74 (0.09)	1.09 (0.07)	bdl	bdl	n.d	bdl		bdl		
Total	99.06 (0.74)	98.99 (0.49)	99.50 (0.52)	99.58 (0.44)	100.28 (0.63)		98.95	99.62	99.60(0.19)		100.81 (0.81)	100
Trace elements (ppm)												
Li	9.90 (1.26)	10.70 (1.13)	13.03 (1.85)	16.79 (0.58)	2.63 (0.16)	6.8	1.1	bdl	1.67 (0.67)	bdl	4.10 (0.86)	
Sc	33.79 (0.60)	33.60 (0.91)	31.08 (1.76)	27.46 (0.69)	13.95 (0.37)	13.7	81	100	133.20 (16.97)	64.8 (0.8)	5.95 (0.98)	
V	270 (6)	283 (17)	302 (19)	369 (6)	4.04 (0.16)	6.26	104	120	259.73 (34.78)	417.67 (35.25)	1.81 (0.35)	3.79 (0.28)
Cr	20.24 (3.22)	23.95 (4.72)	9.27 (2.16)	7.39 (0.67)	36.45 (4.15)	12	5860	3604	530.73 (328.55)	346.67 (80.96)		
Ni	41.16 (1.68)	38.33 (3.02)	25.55 (3.23)	14.61 (1.06)	1193 (13)	677	252	nd	155.68 (7.52)	73.40 (2.05)		
Ga	16.49 (0.66)	16.60 (1.53)	16.72 (1.37)		bdl	bdl	2.5	nd	4.64 (0.69)	8.65 (0.54)	16.76 (2.21)	
Rb	60.94 (2.18)	64.12 (5.80)	90.47 (8.72)	136.07 (3.97)	bdl	bdl	n.d	bdl	bdl	12.73 (3.99)		1.66 (0.38)
Sr	676 (11)	673 (60)	614 (31)	535 (10)	0.02	bdl	69	58	45.23 (1.49)	125.67 (20.03)	1189.80 (52.80)	1360.61 (33.93)
Y	21.50 (0.46)	25.15 (0.99)	27.30 (2.33)	37.26 (1.29)	0.09 (0.011)	0.25	5.9	8	16.42 (2.24)	29.67 (1.33)	0.21 (0.10)	0.29 (0.02)
Zr	123 (2.66)	146 (6)	175 (18.24)	267 (8.41)	0.03 (0.006)	bdl	9	12	31.74 (9.63)	84.37 (10.70)	0.21	

Table 2 (continued)

	Matrix glass				Olivine		Clinopyroxene				Plagioclase	
	Average 3 July 2019 ($n=22$)	Average 23 August 1998 (n = 10)	Average 19 July 2020 (n = 20)	Average sample 17 ($n=13$)	Average ST130-ST305	STPL804b-spot7	STPL804A-113	ST212-PX2-2	Average STPL801 7b (spot86-89)	STPL804A-112	Average STPL801 7b (spot 94–95.104–105.108)	ST212 (Pl7 rim)
	LP (pumice from paroxysm)	LP (pumice from major explosion)	Intermediate (yellow material on scoriae)	HP (scoria)	Ol Fo_{86}	$OlFo_{82.6}$	Cpx (Mg#0.91)	Cpx (Mg#0.87)	Cpx (Mg#0.85)	Cpx (Mg#0.75)	pl An_{90}	pl An_{67}
Nb	13.59 (0.42)	17.66 (1.61)	19.77 (2.22)	31.80 (0.82)	bdl	bdl	bdl	bdl	0.09 (0.04)	3.42 (0.99)		0.04
Cs	3.78 (0.23)	3.92 (0.47)	5.70 (0.57)	8.76 (0.34)	bdl	bdl	n.d	bdl	bdl	bdl		
Ba	831.52 (16.24)	896 (42)	1062 (82.6)	1416.23 (27.05)	bdl	bdl	0.05	bdl	0.29 (0.40)	148.96 (44.31)	124.02 (18.66)	590.28 (10.55)
La	38.51 (0.83)	45.44 (1.22)	52.71 (4.91)	77.92 (1.54)	bdl	bdl	2.0	2.5	2.98 (0.39)	15.29 (2.27)	2.15 (0.32)	6.66 (0.21)
Ce	74.69 (1.44)	87.12 (3.54)	100.4 (9.64)	148.60 (3.38)	bdl	bdl	6.7	8.0	10.89 (1.26)	43.35 (4.49)	3.19 (0.45)	9.73 (0.38)
Pr	8.41 (0.21)	10.40 (0.49)	11.13 (1.09)	16.40 (0.39)	bdl	bdl	1.3	1.5	2.03 (0.20)	6.42 (0.55)	0.31 (0.08)	0.89 (0.02)
Nd	35.02 (0.67)	42.39 (1.93)	44.85 (4.45)	65.63 (2.17)	bdl	bdl	7	8.6	12.35 (1.71)	31.71 (2.24)	1.17 (0.25)	3.01 (0.26)
Sm	6.93 (0.35)	8.18 (0.6)	9.09 (1.19)	12.34 (0.38)	bdl	bdl	1.9	2.7	4.20 (0.52)	8.69 (0.50)		0.35 (0.11)
Eu	1.94 (0.12)	2.20 (0.10)	2.32 (0.27)	2.95 (0.10)	0.01	bdl	0.58	0.6	1.22 (0.15)	2.11 (0.13)	0.39 (0.09)	0.88 (0.01)
Gd	5.94 (0.46)	7.11 (0.50)	7.54 (0.74)	10.15 (0.33)	bdl	bdl	2.1	2.4	4.43 (0.42)	7.93 (0.55)	0.25	0.19 (0.11)
Tb	0.80 (0.05)	0.90 (0.05)	1.01 (0.12)	1.35 (0.07)	bdl	bdl	0.24	0.3	0.64 (0.11)	1.09 (0.06)		0.01 (0.001)
Dy	4.40 (0.21)	5.19 (0.39)	5.28 (0.62)	7.37 (0.31)	0.02 (0.003)	bdl	1.3	1.9	3.68 (0.37)	5.97 (0.23)		0.06 (0.01)
Ho	0.84 (0.06)	0.98 (0.06)	1.03 (0.12)	1.42 (0.06)	0.0043	bdl	0.25	0.34	0.71 (0.12)	1.18 (0.08)		
Er	2.11 (0.10)	2.47 (0.24)	2.66 (0.37)	3.66 (0.16)	0.02 (0.006)	bdl	0.6	0.9	1.68 (0.29)	2.67 (0.06)		
Tm	0.31 (0.04)	0.34 (0.06)	0.37 (0.06)	0.53 (0.04)	bdl	bdl	0.07	0.12	0.23 (0.04)	0.38 (0.03)		
Yb	1.97 (0.20)	2.47 (0.41)	2.46 (0.34)	3.60 (0.21)	0.03 (0.006)	bdl	0.5	0.77	1.35 (0.27)	2.41 (0.17)		
Lu	0.30 (0.03)	0.34 (0.08)	0.39 (0.05)	0.52 (0.03)	0.01 (0.002)	0.025	0.06	0.09	0.19 (0.04)	0.36 (0.03)		
Hf	2.97 (0.16)	3.59 (0.35)	4.28 (0.54)	6.15 (0.31)	bdl	0.081	0.31	0.7	1.69 (0.63)	bdl		
Ta	0.77 (0.05)	1.00 (0.09)	1.14 (0.18)	1.85 (0.07)	bdl	bdl	bdl	bdl	0.02 (0.02)	bdl		
Pb	14.84 (0.63)	17.40 (2.08)	20.82 (2.01)	29.34 (0.61)	bdl	bdl	0.11	bdl	0.11 (0.03)	bdl	1.03 (0.20)	4.12 (0.22)
Th	11.06 (0.36)	12.88 (0.50)	17.32 (1.84)	26.72 (0.81)	bdl	bdl	0.02	0.07	0.10 (0.04)	2.69 (0.74)		
U	2.95 (0.10)	3.32 (0.31)	4.59 (0.55)	7.26 (0.31)	bdl	bdl	bdl	bdl	0.02 (0.01)	bdl		

n number of analyses: in brackets = standard deviation. Fo = Forsterite mol.%, Mg# = MgO/(MgO + FeO), An = Anorthite mol.%. ol = olivine; cpx = clinopyroxene; pl = plagioclase

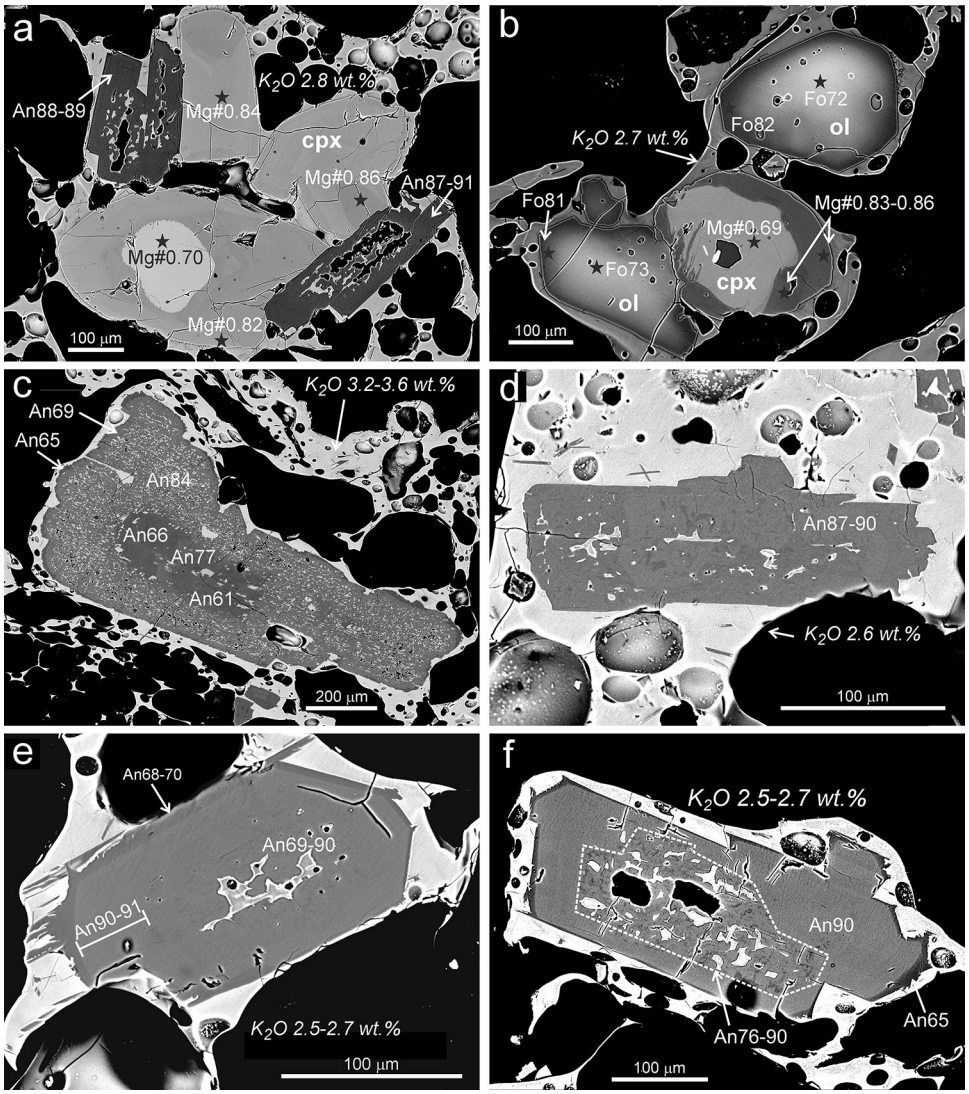

Fig. 4 BSE images of the mafic minerals hosted in the highly vesicular material of the 19 July 2020 products (ST801 and 804). **a** Aggregate of euhedral clinopyroxene Mg# 0.82–0.86 (Fs_8), with resorbed core Mg# 0.70 (Fs_{18}), and plagioclase $An_{87–91}$ hosting large vesicles and melt inclusions at the core. **b** Aggregates of rounded to euhedral olivine with resorbed cores $Fo_{72–73}$ and more magnesian rims ($Fo_{81–82}$), and clinopyroxene crystals with resorbed core Mg# 0.69 (Fs_{19}) and magnesian mantle Mg# 0.83–0.86 ($Fs_{8–9}$) **c** Plagioclase phenocryst with resorbed, zoned core (An_{66-67}) encircled by a sieve textured, An-rich corona (~ An_{84}) and an external rim < 10 µm ~ An_{65-69}. **d** Patchy zoned plagioclase $An_{87–90}$, hosting melt inclusions and small vesicles. (**e** and **f**) Plagioclase microphenocrysts with patchy zoned cores $An_{69–90}$ hosting large melt inclusions and vesicles, encircled by undisturbed layer $An_{90–91}$ and external rims < 10 µm ~ $An_{65–70}$. Compositions of olivine (ol), clinopyroxene (cpx) and plagioclase (pl) are given as Fo mol.%, Mg# (Mg/Mg + Fe) and An mol.%, respectively. The composition of the glass adhering to the crystals is given as K_2O wt.%

trace elements) measured in the intermediate glasses can overlap the field of those of both the LP and HP melts, we decide to maintain this separation, also to be consistent with other studies (Bertagnini et al. 2008 and references therein).

LP glasses

LP pumices ($K_2O < 2.4$ wt.%) analyzed in this work show systematic differences in glass chemistry, both as major and trace element contents (Fig. 5a-–d; Table 2). In particular, in the K_2O vs CaO binary diagram (Fig. 5a), products from major explosions and paroxysms occupy two distinct fields, partially overlapped, at high K_2O and low CaO and low K_2O and high CaO, respectively. Pumices erupted during the paroxysms of 2003, 2007, and 2019 cover the same field of variability in terms of major elements. They are characterized, on average, by CaO 10.8–11.9 wt.% and K_2O 1.7–2.2 wt.% contents. Major explosions occurred in the period between 1998 and 1999, and on 24 November 2009, there have groundmass composition ranging within CaO 10.4–11.2 wt.% and $2.1 < K_2O < 2.4$ wt.% (Fig. 5a). Among the other major elements, NaO, SiO_2 and FeO increase in melts from paroxysms to major explosions, while MgO and Al_2O_3 decrease; TiO_2 and P_2O_5 remain quite constant. Although the observed compositional differences are small, they are larger than the analytical errors, and are also highlighted by the trace element contents. Indeed, incompatible trace elements (e.g., Nb, Zr, Ta, Th) show increasing concentration from the matrix glasses of the paroxysms to the major explosions (Fig. 5b, c; Online Resource 1). Ni, V, and Sc compatible with olivine and clinopyroxene have different behavior, where a strong decrease in Ni from paroxysms to major explosions is observed, while Sc and V remain quite unchanged. Another important result concerns the variation of Cr, compatible with the pyroxene structure, that is systematically more abundant in products from 2007 paroxysm

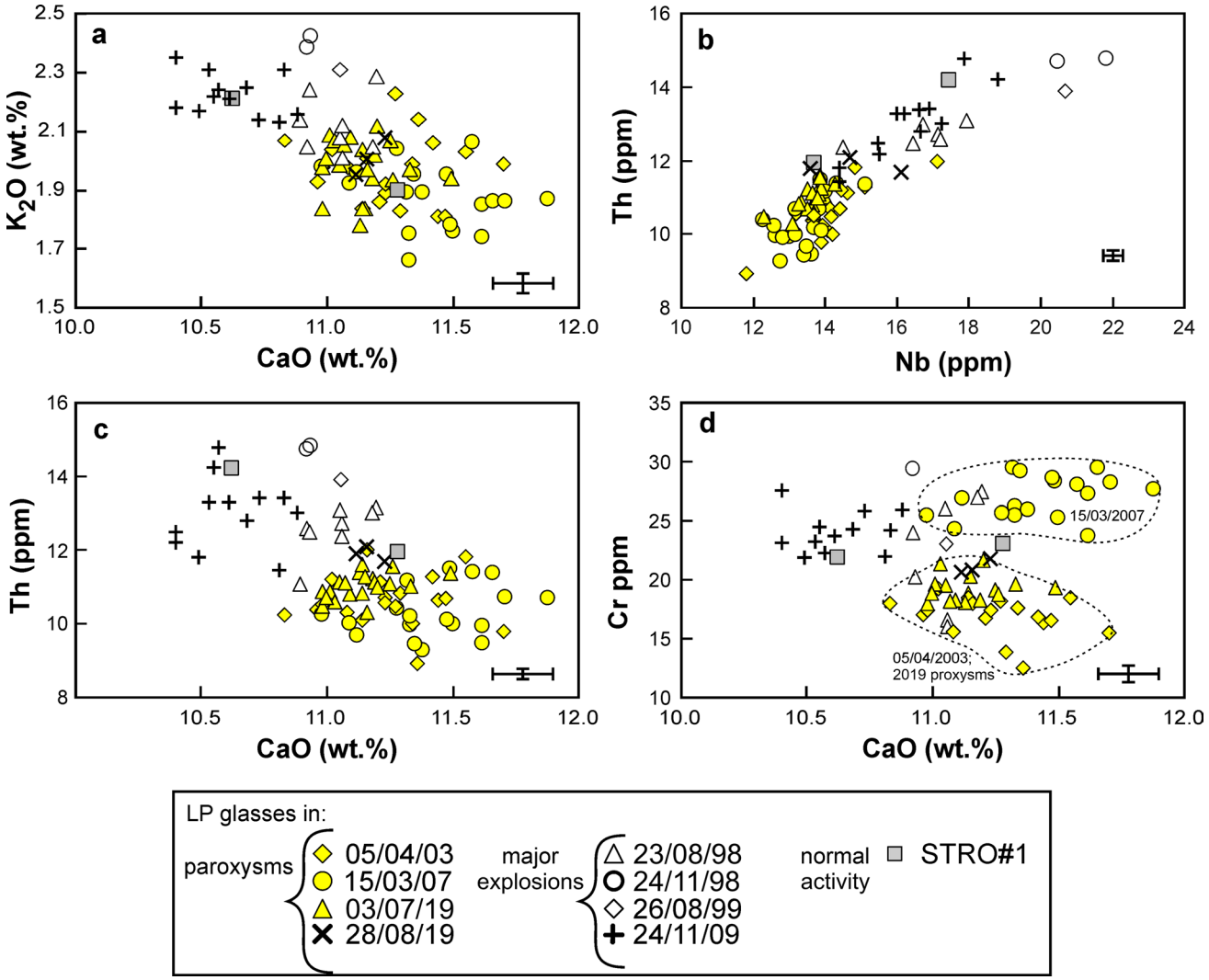

Fig. 5 Bivariate diagrams showing the variation of representative major and trace elements in matrix glasses from LP pumices erupted during paroxysms and major explosions. Glasses of pumice from major explosions show higher contents of K_2O (**a**) and incompatible trace elements (**b**, **c**) than those of the paroxysms. **d** The two distinct compositional fields of the 15 March 2007 paroxysm and 5 April 2003 and both 2019 paroxysms are marked by dotted lines. Error bars correspond to 2*RSD%

(Cr = 23.7–29.4 ppm) with respect to the pumices emitted in the 2003 and both 2019 paroxysms (Cr = 12.5–21.8 ppm; Fig. 5d). Pumices from 1998 to 1999 major explosions cover almost the whole range of variation (Cr = 16.3–29.4 ppm) depicted by paroxysms, while products from 24 November 2009 (Cr = 21.9–27.6 ppm) show a decreasing trend of Cr content, starting from the most evolved 2007 products. Two ash fragments from the October 2019 normal activity (STRO#1) have groundmass glasses with textural and compositional features covering the same range of LP pumices erupted during the 24 November 2009 and 28 August 2019, major explosion and paroxysm, respectively.

Intermediate compositions

Groundmass glasses with intermediate composition (2.5 wt.% < K_2O < 3.8 wt.%) between LP and HP end-members (INT in Table 1) show different ranges of variation in terms of both major and trace element content (Table 2). These melts are often associated with intra-clasts chemical heterogeneities at the micrometer scale, defining a continuum between the composition of the HP and LP glassy matrices, well documented in both 2019 paroxysms (Andronico et al. 2021) and in some major explosions (e.g., 8 November 2009; Landi and La Felice 2011a). In these cases, the intermediate compositions cover the whole range of CaO/Al_2O_3 ratios between 0.48 and 0.63. Also, they follow linear trends due to mixing/mingling between the LP and HP end-members

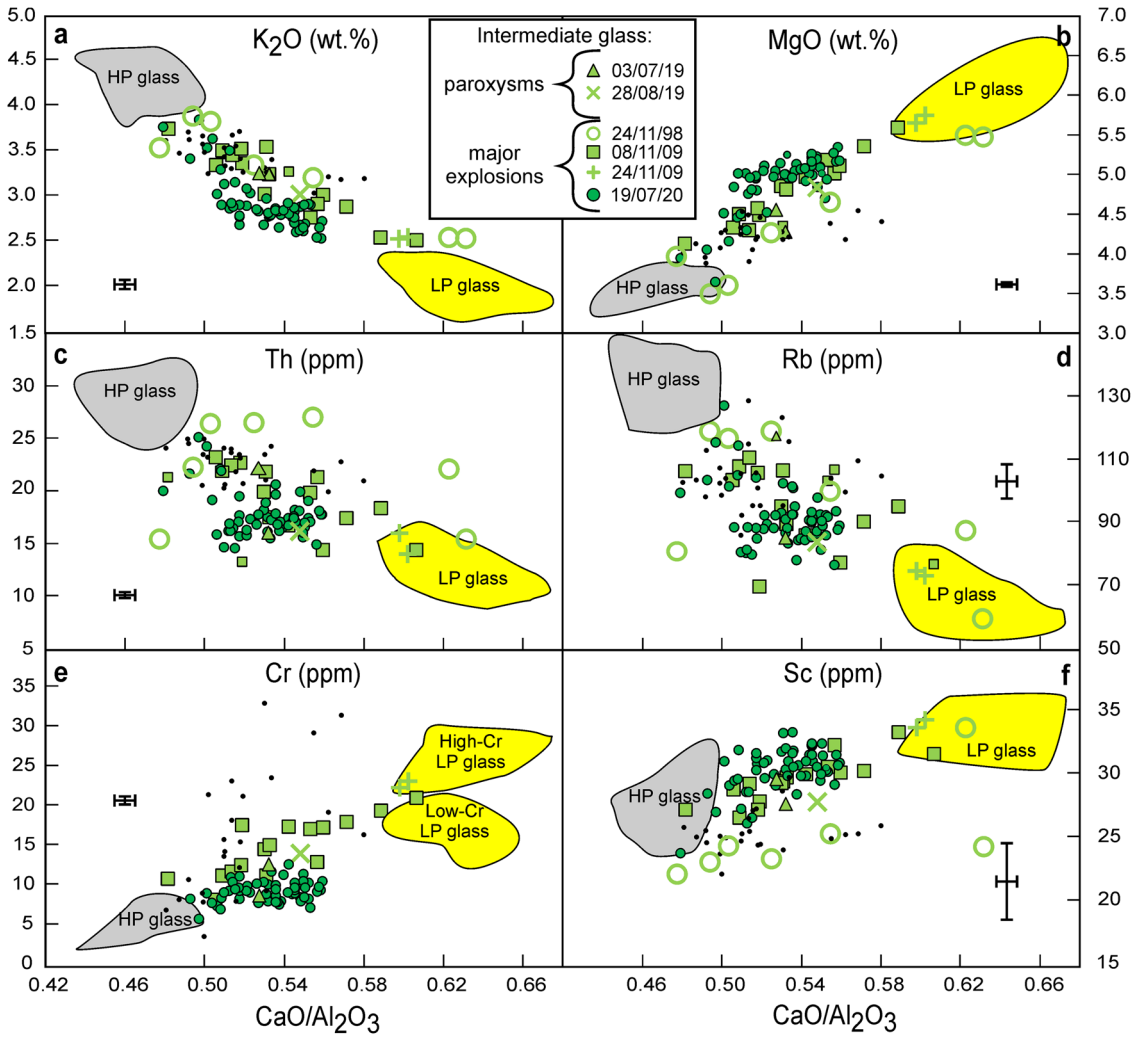

Fig. 6 Variation of selected incompatible (K_2O, Th and Rb) and compatible (MgO, Cr and Sc) major and trace elements with respect to CaO/Al_2O_3 ratio, in matrix glasses with chemical composition intermediate between LP and HP end-members, from the products emitted during major explosions and paroxysms. The composition of the LP and HP end-members are reported as fields of variation (LP: yellow; HP: gray). Black dots: 9 January 2005, data from Landi et al. (2008). Error bars correspond to 2*RSD%

(Fig. 6a–f). The sample related to the 8 November 2009 major explosion shows an evolved LP glass composition and it is strongly mingled with the HP melts; typical LP end-member ($K_2O < 2.4$ wt.%) is rare or absent in this sample, as previously reported by La Felice and Landi (2011a). Different trends are detected in groundmasses from the "high-energy explosion" that occurred on 9 January 2005 (Landi et al. 2008) and the major explosion of 19 July 2020 (present work), in which the groundmass glasses have a similar range of variations for major oxides, characterized by a compositional gap with the LP end-member. Despite this similarity, most of the intermediate compositions related to the 19 July 2020 are clustered within a homogeneous field characterized by CaO/Al_2O_3 of 0.51–0.56 wt.%, K_2O of 2.5–3.0 wt.%, and MgO of 4.7–5.3 wt.% (Fig. 6a, b). Incompatible trace elements (Th, Rb) in the products of 19 July 2020 show a slightly negative correlation with CaO/Al_2O_3, in the range of Th = 14.5–19.8 ppm and Rb = 79.5–97 ppm (Fig. 6c, d), while compatible elements are on a horizontal trend (Fig. 6e, f). Samples from 8 November 2009 and 19 July 2020 major explosions show a different correlation of Cr vs CaO/Al_2O_3 (Fig. 6e): in the first case, there is a continuum decrease from the more evolved glass measured in products from 24 November 2009 toward the HP compositional field (Cr = 11.2–21.1 ppm), while the matrix glasses from 19 July 2020 have a quite constant Cr content, around 10 ppm.

HP glasses

Major elements in the HP glasses (K_2O 3.9–4.5 wt.%) cover the same compositional range reported in the literature (Table 2) with only small differences among the products erupted during normal, major and paroxysmal activities (Landi et al. 2004, 2011). Incompatible trace elements (e.g., Rb, Zr, La, Ce, Y, Th, Ta) and Sr (compatible in plagioclase) show ranges of variation within 8–12%, close to the analytical error (< 10%). Only Ni (7–15 ppm) and Cr (2–10 ppm) show larger variations (Table 2; Online Resource 1).

Discussion

Inferences on the intermediate zone of the plumbing system from mineral chemistry

Products with intermediate composition erupted during the 19 July 2020 major explosion are characterized by heterogeneous mineral chemistry. The Fe-rich compositions measured at the core of many mafic crystals (e.g., cpx Mg# 0.69–0.73; ol $Fo_{70–73}$; Fig. 4a, b) can be considered as the remnant of a dissolved crystal belonging to a vertically extended crystal mush developed either during the present activity or in the previous periods (Francalanci et al. 2005, 2012; La Felice and Landi 2011b; Di Stefano et al. 2020; Andronico et al. 2021), and carried off by the magma during its ascent toward the surface. Based on the habit, euhedral rims of clinopyroxene crystals with Mg# 0.82–0.86 ($Fs_{8–10}$) associated with olivine rims $Fo_{81–82}$ seem to be in textural equilibrium with a matrix glass with K_2O 2.6–2.7 wt.% content. Adopting a partition coefficient for Fe–Mg exchange between pyroxene and melt ($K_D^{cpx-liquid}$) between 0.22 and 0.24, as suggested by experimental studies (Conte et al. 2006; Di Carlo et al. 2006), pyroxene with composition Mg# = 0.80–0.82 ($Fs_{9–10}$) is in chemical equilibrium with the glass K_2O = 2.6–2.7 wt.% (Mg# 0.50). Similarly, olivine $Fo_{81–83}$ is in chemical equilibrium with the same glass, assuming a $K_D^{ol-liquid}$ of 0.27–0.3 and a Fe^{3+}/Fe^{2+} ratio of 0.22–0.27 (at oxygen fugacity of NNO + 0.5 and NNO + 1) (Di Carlo et al. 2006; Pichavant et al. 2009). In addition, plagioclase microphenocrysts with composition $An_{87–91}$, also found in aggregates together with cpx Mg# 0.82–0.86 ($Fs_{8–9}$), grow in textural equilibrium with the same intermediate glasses.

The occurrence of microphenocrysts of plagioclase with nearly homogeneous composition An_{90} is the most relevant result that emerges from the mineralogical investigation. As reported in the large literature focused on the products of the persistent activity at Stromboli (Bertagnini et al. 2008 and references therein), the compositional range of plagioclase is between An_{60} and An_{90}, thus including high-calcium end-members ($An_{88–90}$). However, the An-rich compositions were sporadically detected and always as skeletal rims and/or microlites (tens of microns) in LP pumices, or as patchy zoned layers and cores in the phenocrysts from the HP products (Francalanci et al. 2004; Landi et al. 2004; Pichavant et al. 2011). These textures and compositions of plagioclase were related to processes of dissolution/crystallization during complex plagioclase–melt interaction mechanisms under decompression (Landi et al. 2004; Pichavant et al. 2022). Conversely, plagioclase microphenocrysts $An_{87–91}$ found in the 19 July 2020 intermediate products present undisturbed layers up to 150 µm thick pointing to an event of nearly equilibrium crystallization.

The field of stability and composition of the plagioclase strongly depends on the water content dissolved in the melt, being the An-rich compositions favored at high water content (Di Carlo et al. 2006; Agostini et al. 2013). Equilibrium crystallization and decompression experiments, carried out under water-saturated conditions using the HK basaltic pumice from Stromboli as starting material (CO_2 free), suggest that An-rich plagioclase enters into this basaltic system at a pressure between 75 and 50 MPa and water content < 2.4 wt.%, at a temperature between 1075 and 1100 °C (Di Carlo et al. 2006; Agostini et al. 2013). Plagioclase does not crystallize at 100 MPa in H_2O- and CO_2-bearing, near-liquidus experiments performed at 1150 °C (that is the temperature estimated for the LP magma) with 2.2–2.5 wt.% of H_2O dissolved in the melt (Pichavant et al. 2009). The anorthite content in the experimental plagioclase, including plagioclase–melt interaction experiments presented in Pichavant et al. (2022), is always lower than An_{90} (An ≤ 85 mol.%), although the equilibrium residual melts have intermediate composition with K_2O between 2.6 and 3.5 wt.% that encloses the 19 July 2020 glass compositions. Based on the experimental results, we can infer that the magmas with intermediate composition hosting plagioclase $An_{87–91}$ emitted during the 19 July 2020 major explosion resided in the lower part of the intermediate zone of the plumbing system that extends between 100 MPa and the bottom of the HP magma body (~50 MPa). The texture at the cores of the An-rich microphenocrysts (Fig. 4e, f) differs from the "reaction textures" found in the mineral/melt interaction experiments, for the occurrence of large bubbles and large melt inclusions, and is better explained with a rapid growth under degassing (Landi et al. 2004). Therefore, the crystallization of microphenocrysts of plagioclase was maybe favored by an event of rapid nucleation under decompression from LP melt storage zones to ~ 50–100 MPa (2–4 km) (growth of patchy zoned, bubble-rich cores $An_{70–90}$), followed by the crystallization of An_{90} plagioclase at nearly equilibrium conditions. Using growth rate (G_L) values of 10^{-7}–10^{-8} cm/s calculated by Agostini et al. (2013) for plagioclase, the residence time

necessary for 100 µm An_{90} microphenocrysts (Fig. 4e, f) to grow ranges from ~1 to 11 days. These must be considered as minimum values because G_L was experimentally obtained under decompression, thus at relatively high undercooling and rapid growth.

Petrogenetic processes and melts evolution

The origin of the compositional variations measured in matrix glasses was investigated by Rayleigh fractional crystallization equations and mass balance calculations using PETROMODELER excel spreadsheet (Ersoy 2013) for the trace element composition. The partition coefficients ($K_D = C^{mineral}/C^{melt}$, where C is the concentration in ppm) for clinopyroxene, olivine, and plagioclase in equilibrium with LP, intermediate, and HP melts, were calculated using average composition of the matrix glasses, and the rims of phenocrysts (Table 3; Online resource 1). The resulting partition coefficients obtained in this work fall in the range of mineral/melt K_D obtained in experiments and for phenocryst/matrix pairs (GERM database; https://earthref.org/KDD-old/). The only exception concerns Chromium, which is one order of magnitude higher for the clinopyroxene in equilibrium with LP melts (Fs_7 in Tables 2 and 3). Although trace element data on cpx $Fs_{5–8}$ are not available from the literature, we consider this result realistic since minerals in equilibrium with HP analyzed in this work have trace element content fully comparable with data published on products with similar composition (Ubide et al. 2019) and also because, in both the analytical sessions of 2001 and 2021, the cpx $Fs_{5–8}$ have a Cr content within the same range of variation (3800–5080 ppm, Online resource 1).

Table 3 Partition coefficients (K_D) of selected trace elements between mineral and matrix glasses of the LP, intermediate and HP products. Mineral and matrix glasses composition in equilibrium are the same reported in Table 2

	LP products from paroxysms						
Element	Ol (Fo_{86})	Cpx (Mg#0.87)		Matrix glass	K_D^{ol}	K_D^{cpx}	
Ba	bdl	n.d		851	< 0.0001	n.d	
Sr	< 0.0001	58		667	< 0.0001	0.09	
Th	bdl	0.07		11.4	< 0.0001	0.006	
Zr	bdl	12		126	< 0.0001	0.1	
Cr	36.45	3604		18.1	2.0	199	
Ni	1193	n.d		40	29.8	n.d	
Nd	bdl	8.6		34.1	< 0.0001	0.25	
	Intermediate products from 19 July 2020						
	Ol ($Fo_{82.6}$)	Cpx (Mg#0.85)	Pl (An_{90})	Matrix glass	K_D^{ol}	K_D^{cpx}	K_D^{pl}
Ba	Bdl	0.29	124.02	1062	< 0.0001	0.0002	0.117
Sr	bdl	45.23	1189.80	614.5	< 0.0001	0.07	1.93
Th	bdl	0.10	Bdl	17.32	< 0.0001	0.006	< 0.0001
Zr	bdl	31.74	0.21	175.25	< 0.0001	0.18	0.001
Cr	12	530.73	Bdl	9.27	1.3	57	< 0.0001
Ni	677	155.68	2.40	25.22	26.8	6.1	0.095
Nd	bdl	12.35	1.17	44.85	< 0.0001	0.27	0.03
	HP products from all eruption styles						
	Ol (Fo_{71})*	Cpx (Mg#0.75)	Pl (An_{67})	Matrix glass	K_D^{ol}	K_D^{cpx}	K_D^{pl}
Ba	155.33	0.58	590.28	1416.23	0.1	0.0004	0.4
Sr	68.87	70.90	1360.61	534.77	0.12	0.13	2.5
Th	2.54	0.26	0.0045	26.72	0.09	0.01	0.0002
Zr	30.73	69.20	Bdl	267.02	0.11	0.26	< 0.0001
Cr	5.46	222	Bdl	7.39	0.74	30	< 0.0001
Ni	315.33	bdl	Bdl	14.61	21.6	< 0.0001	< 0.0001
Nd	6.93	33.70	3.01	65.63	0.1	0.5	0.05

Fo = Forsterite, Mg# = MgO/(MgO + FeO), An = Anorthite mol.%. ol = olivine; cpx = clinopyroxene; pl = plagioclase

*Average analysis from Landi et al 2004

LP melts

The LP magma deep system has been the object of several works in the past decades that point to a model represented by a dyke-like feeding system that extends between 6 and 9 km, characterized by repeated refilling from depth followed by magma mixing, minor crystallization of mafic minerals and assimilation of deep cumulates (Pichavant et al. 2009, 2011; Schiavi et al. 2010; Pompilio et al. 2012; Métrich et al. 2010, 2021).

In our data set, the pumice from the 15 March 2007 paroxysm shows the higher content of Cr (Cr > 24 ppm), the LP products erupted on 5 April 2003 and 3 July 2019 paroxysms have low Cr contents (Cr < 20 ppm), and products of the 28 August 2019 paroxysm have intermediate Cr values (Figs. 5d). We point out that among the violent explosions analyzed, the paroxysms with highest intensities are fed by Cr-poor magmas that are possibly less contaminated by processes of cumulate assimilation. This aspect, out of the scope of the present work, needs to be further investigated to establish if the highest intensity paroxysms associated with lower cumulate assimilation (low Cr) can be related to fast magma ascent from deep sources.

Another relevant point concerns the compositional differences observed in the erupted tephra emitted during major explosions and paroxysms (Figs. 5, 7) that were also detected by Pioli et al. (2014), based on the major element analyses of the matrix glass. In the diagram Th/Nd vs Th (Fig. 7a) the less evolved glasses, corresponding to samples from paroxysms with $K_2O < 2.1$ wt.%, follow a mixing line between the less and more evolved end-members with Th 9.3 ppm and 11.6 ppm, respectively, where the glasses from 3 July 2019 occupy the field at highest values (10.3–11.6 ppm). Conversely, the chemical variations measured in the 28 August 2019 paroxysm and the major explosions deviate from the mixing line, and are well fitted by a model of fractional crystallization, explained by less than 15 vol.% of cpx (± ol), starting from LP glasses erupted in paroxysms with variable Th/Nd ratios (Fig. 7b). However, the differences in Cr and Ni content in the matrix glasses of pumiceous LP products are not consistent with a simple crystal fractionation of clinopyroxene and olivine. These variations, which were associated with different extents of assimilation of gabbroic cumulates at depth (Pichavant et al. 2009; Schiavi et al. 2010), combined with crystal fractionation, seem to persist even in the products of major explosions following the paroxysm. In fact, after 2007, the two major explosions of November 2009 are perfectly aligned with the evolutionary trend starting from the LP products emitted on 15 March 2007, and similarly, the Cr and Ni contents of the glasses erupted on the 19 July 2020 major explosion have intermediate values between the LP pumices of the 2019 paroxysms and the field of variation of HP glasses from the

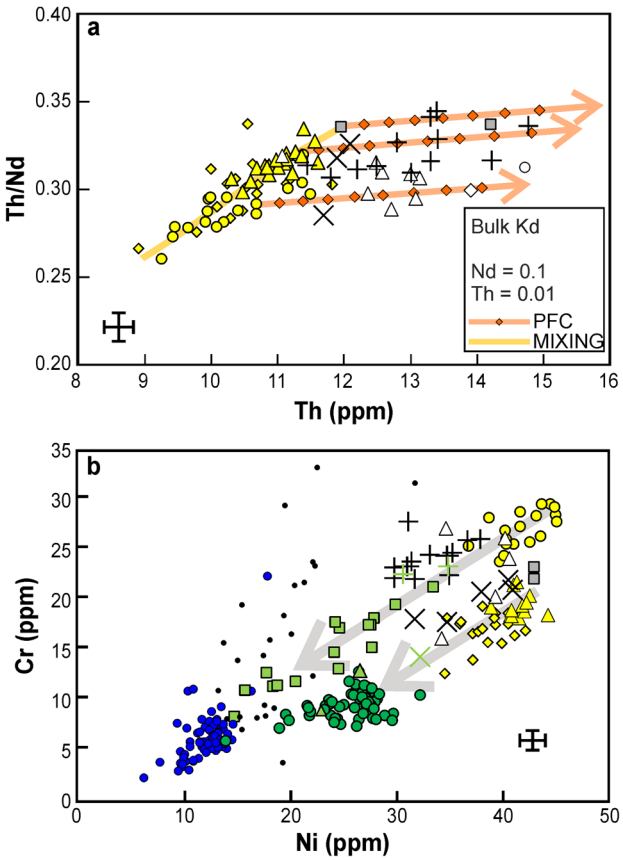

Fig. 7 **a** Plot of Th/Nd versus Th for matrix glasses from LP pumices. The data define arrays that are consistent with a mixing between products of paroxysms, and different degree of crystal fractionation (PFC) for products of major explosions starting from LP pumices with variable Th/Nd ratio. Products from the 28 August 2019 paroxysms show a slightly evolved matrix composition, consistent with a 2–6 wt.% of PFC starting from the products of the 3 July 2019 paroxysm. Two analyses obtained on pumiceous products from the 1 November 2019 (STRO#1) normal activity show evolved LP composition, in agreement with the high intensity level of the normal activity in the months shortly following the summer 2019 paroxysms. Partition coefficients of highly incompatible trace element (Th, $K_D < 0.01$) and moderately incompatible trace element (Nd, $K_D = 0.1$) correspond to bulk K_D, obtained assuming a mineral assemblage made up of 90 wt.% of cpx and 10 wt.% of ol. Each point on the PFC array corresponds to a 2% of increment of crystallization. **b** Plot of Cr versus Ni for matrix glasses from all the studied eruptions. The gray arrows outline the two different evolutionary trends from high- and low-Cr paroxysms toward the following major explosions (see text for detail). The two trends converge in the HP products, without further distinction. Symbols as in Fig. 1. Black dots: 9 January 2005, data from Landi et al. (2008)

normal activity (Fig. 7b). Considering that there is not a clear relationship between the bulk rock composition and the intensity of the explosion (Pompilio et al. 2012; Métrich et al. 2021), the evolved glasses found in LP products from major explosions should be related to a higher crystal content of the magma, likely induced by lower volatile contents/

lower temperature at relatively lower pressure. Although the LP products are generally crystal poor, small differences in the degree of melt evolution due to crystallization among the erupted products are consistent with the results from melt inclusions in olivine that point to a vertical and chemical zoning of the deep feeding system (Bertagnini et al. 2003; Métrich et al. 2010). Moreover, the chemistry of the matrix glass agrees with the lower content of Fo (mol.%) in the outer rim of the olivine from major explosions compared to those of the paroxysms (Métrich et al. 2001, 2021).

The depth of the LP reservoir is reported at 190–250 MPa (about 6–9 km), based on the total fluid pressure ($P_{H2O} + P_{CO2}$) recorded by melt inclusions (Métrich et al. 2010, 2021). H_2O and CO_2 have been measured only in melt inclusions hosted in olivine from pumices erupted during paroxysms (both small and large), so it cannot be excluded that the LP feeding system can extend at a relatively shallower depth. Since LP magmas are distinct from intermediate or HP magmas by the absence of plagioclase, following the previously discussed experimental results, the top of the LP reservoir might be located at a pressure up to 100 MPa. We propose that the LP deep reservoir develops a vertical zoning in terms of chemical compositions of the liquid phase and crystal content, producing a slightly more evolved cap, or pockets of more evolved magma located in the upper portion of the deep feeding system. During the paroxysms, the gas-rich magma rises from the deepest portions of this dike-like reservoir, while major explosions are suggested to involve only the shallower portions. Alternatively, the magma feeding the major explosions can represent the feeding zone of the HP reservoir, which is continuously hybridized by regular arrivals of the LP magmas, as suggested by Pioli et al. (2014). However, the continuum evolutionary trend modeled by simple fractional crystallization, starting from the LP melts found in paroxysms, is in better agreement with the suggestion of a vertical zoned LP reservoir. Here, minor degassing, possibly accompanied by a small decrease in the temperature, can induce minor crystallization of mafic minerals. Additional studies focusing on these evolved LP magmas are necessary to better position and define the upper part of the LP reservoir.

Intermediate melts

The large variability measured within the studied glasses with intermediate compositions between LP and HP end-members can be ascribed to different petrogenetic processes, with particular reference to mixing and mixing + crystallization. In the CaO/Al_2O_3 vs FeO/MgO diagram, intermediate compositions measured in samples from the 8 November 2009 major explosion cover the whole range between the two end-members (Fig. 8a). As shown in previous studies focused on this eruption, these intermediate compositions

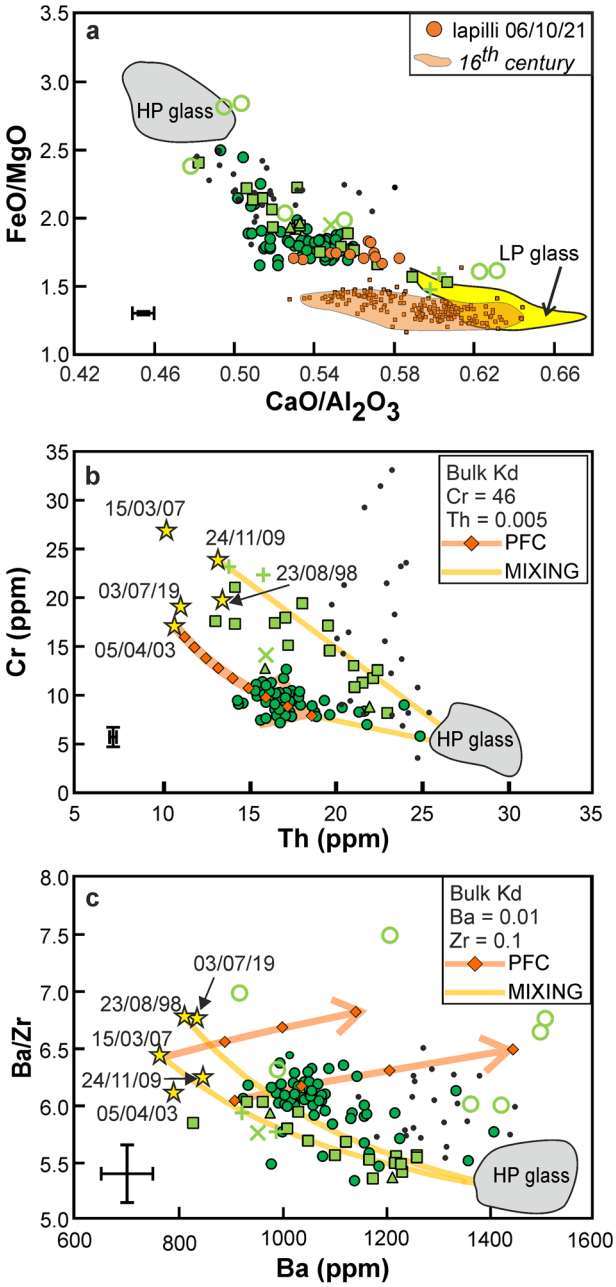

Fig. 8 **a** Plot of matrix glasses from all the studied products in the FeO/Mg versus CaO/Al_2O_3 ratios field of variations. Analyses obtained in this work are compared with the analyses of La Felice and Landi (2011a, b) on products from a paroxysm occurred at Stromboli around the sixteenth century. Preliminary analyses of pumiceous fragments emitted during the last major explosion occurred at Stromboli on 06/10/2021 are also shown. **b** and **c** Plots of **b** Cr versus Th and **c** Ba/Zr versus Zr for matrix glasses of all the studied products and trace element modeling for both mixing and crystal fractionation (PFC) processes. The averaged glass composition (yellow stars) of the 15/03/07 (**b** and **c**) and 03/07/19 (**c**) is considered as the least evolved end-members for the mixing process with HP products. Crystal fractionation (PFC) arrays are obtained considering bulk K_D of a mineral assemblage made up of 80 wt.% of cpx (±10 wt.% of ol) + 10 wt.% of pl. Each point on the PFC array corresponds to a 2% (**b**) and 10% (**c**) of increment of crystallization. In both the plots (**b**) and (**c**), the intermediate products from the 08/11/09 and 19/07/20 major explosions follow the mixing and PFC trends, respectively. Symbols as in Fig. 1. Black dots: 9 January 2005, data from Landi et al. (2009)

can be interpreted mostly as magma mixing at different degrees of hybridization (La Felice and Landi 2011a; Andronico et al. 2021; Pioli et al. 2014). Trace element modeling indicates that they can be approximated by mixing processes (Fig. 8b, c), in particular between Cr-rich melts, as that erupted on 15 March 2007, and HP melts (Fig. 8b). Conversely, the relatively evolved intermediate compositions measured in the products of the 9 January 2005 high-energy explosion have been interpreted as related to mixing and/or mineral dissolution due to rehydration of the sinking HP degassed magma and its re-equilibration at higher water pressure (Landi et al. 2008; Pioli et al. 2014). The scattered Cr and Ba contents in glasses from 9 January 2005 shown in Fig. 8 agree well with the invoked process of mineral dissolution.

In Fig. 8a the intermediate glasses of the products erupted on the 19 July 2020 major explosion deviate from the mixing lines, following a trend parallel to the CaO/Al_2O_3 axis (between CaO/Al_2O_3 0.51–0.56 and FeO/MgO 1.6–1.8). A few lapilli erupted in a recent major explosion that occurred on 6 October 2021 (only major element composition available) have a glassy matrix with nearly homogeneous and intermediate compositions close to that of the 19 July 2020 products (CaO/Al_20_3 0.53–0.57; FeO/MgO 1.7–1.8; K_2O 2.5–2.8 wt.%) that line up on the same trend. A parallel trend was previously detected in the products erupted during the historical, large paroxysm that occurred in the sixteenth century (Fig. 8a) (Bertagnini et al. 2011; La Felice and Landi 2011b). In this case, the horizontal trends start from LP compositions and are related to clinopyroxene crystallization (La Felice and Landi 2011b). Chemical modeling indicates that the 19 July 2020 intermediate glasses can be reproduced by superimposing mixing processes and fractional crystallization (Fig. 8b, c), where the LP end-member involved is likely similar to that erupted on 5 April 2003 and 3 July 2019 paroxysms, in terms of Cr and Ni content (Fig. 8a). More in detail, in Cr vs Th diagram, results of Rayleigh crystallization, performed using the K_D of intermediate mafic paragenesis, indicate that less than 10 wt.% clinopyroxene and olivine drive the residual melts to the 19 July 2020 intermediate glass domain (Fig. 8b). The trend of variation of Ba/Zr vs Ba suggests that the intra-eruption glass variability can be accounted by a < 15 wt.% of crystallization that involves mainly pl and cpx ± ol, in variable proportions (Fig. 8c). Accordingly, plagioclase starts to become the dominant mineral phase in these intermediate melts, as confirmed by the occurrence of euhedral microphenocrysts of anorthite-rich plagioclase.

It should be noted that in all the graphs presented, a more or less significant dispersion of the points plotted is observed. Indeed, the whole feeding system at Stromboli, from the deep LP reservoir to the shallow conduits, is largely dominated by mixing processes due to continuous refilling and degassing (Landi et al. 2004, 2008; Métrich et al. 2021). According to Perugini et al. (2006, 2008), extensive and continuous chaotic mixing may induce a "diffusive fractionation" process leading to melts heterogeneity and large dispersion of the trace element values. Dispersion can be also produced by local enrichment/depletion of trace elements due to disequilibrium crystallization during ascent and degassing.

HP melts

The HP glasses analyzed fall within a rather narrow chemical interval, K_2O 3.9–4.4 wt.% and CaO 6.8–7.8 wt.% (Fig. 9a). The observed systematic differences, both in major and trace elements, of the HP scoriae emitted during explosions with different intensities, can be modeled with a minor extent of crystallization (< 20%) of a solid composed of the same minerals observed as modal crystals, in which plagioclase dominates over mafic minerals and vice versa (Fig. 9b, c), depending on how much cooling (plus clinopyroxene and olivine) or degassing (plus plagioclase) affect the crystallization process. Indeed, the P–T field of stability of cpx in basaltic magmas covers a lower and wider temperature range than plagioclase (Bamber et al. 2020). Interestingly, HP glasses mingled with LP material in products from paroxysms show the more evolved compositions, as also highlighted by the comparison with major element analyses of products from the normal activity between 2005 and 2008 (Landi et al. 2011). This is consistent with the involvement of large portions of the shallow HP reservoir during the high-energy paroxysmal activity, including also the cooled and crystallized portions at the conduit walls.

Another important consideration concerns the Cr and Ni content of HP products. In the diagram Ni vs Cr (Fig. 7b), the Cr-rich and Cr-poor trends, depicted by LP and intermediate magmas, converge into a rather tight HP area, where the different Cr contents of glasses with a comparable evolutionary degree are no longer recognizable. Continuous refilling, crystallization, and mixing within the shallow system can obliterate, in the residual matrix glass, the geochemical fingerprints of the primary magmas.

Insights into the magmatic plumbing system

The results discussed above are in agreement with a dike-like magma system that evolves from the deep, volatile-rich LP to the shallow, volatile-poor HP end-members through several petrogenetic processes, among which mixing and crystallization play the main roles. The compositional characteristics of the products erupted during the different styles of activity allow the reconstruction of a vertically zoned plumbing system, in terms of matrix glass composition, glass heterogeneity, and crystal content and composition

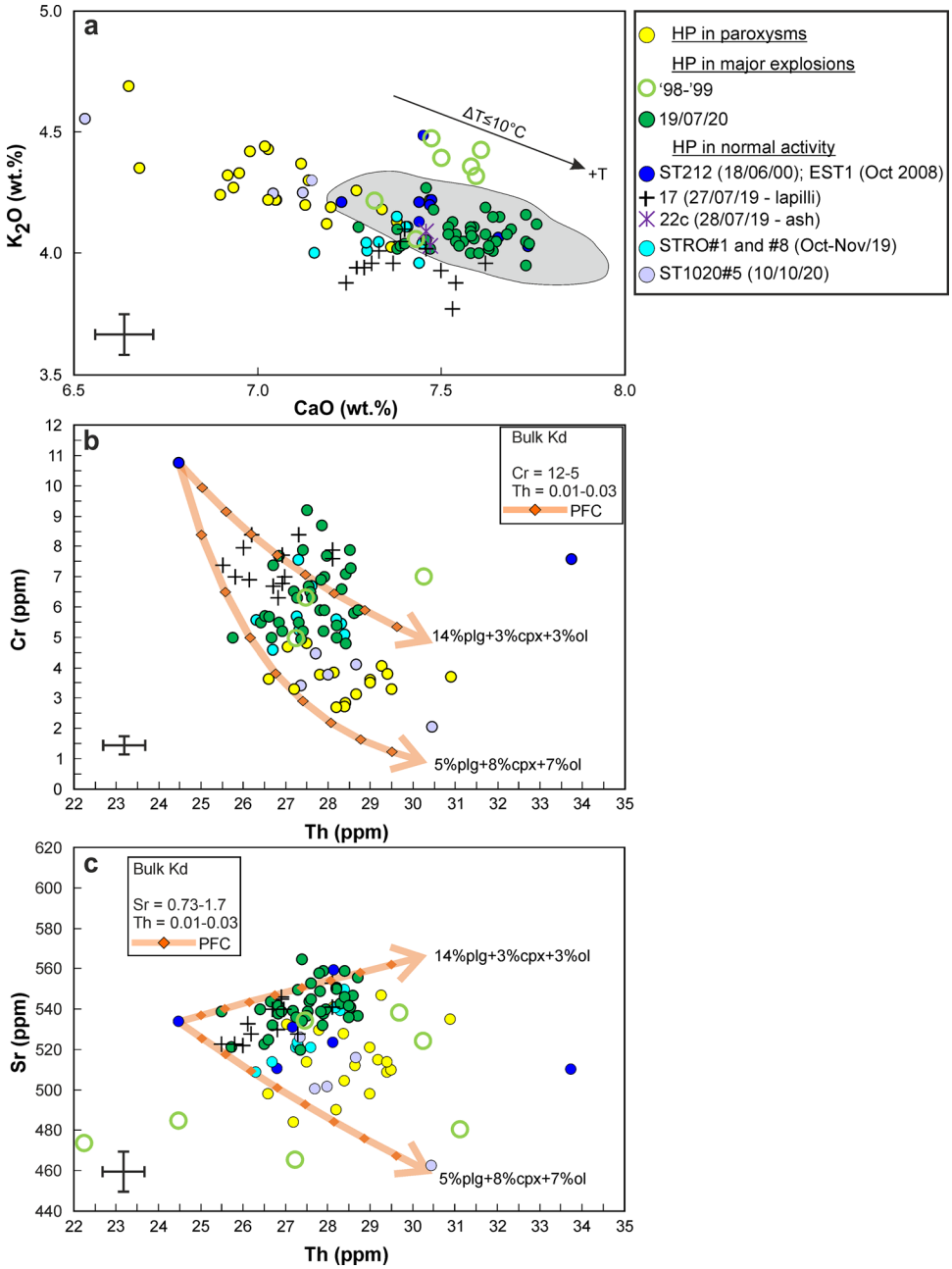

Fig. 9 Matrix glasses in HP scoriae (fragments of bombs, lapilli and ash) erupted during the whole range of eruption intensity occurred at Stromboli in the past 22 years. **a** Plot of major elements K_2O versus CaO, and comparison with the compositional field of variation (gray field) of Landi et al. (2011) interpreted as a difference in magma temperature of less than 10 °C (arrow). **b** and **c** Trace element modeling of the observed variations as crystal fractionation (PFC) assuming a range of bulk K_D consistent with a mineral assemblage made up of 14%pl + 3%cpx + 3%ol and 5%pl + 8%cpx + 7%ol, respectively

(Fig. 10). An accepted model of the LP portion of the plumbing system indicates that the magma involved in the paroxysms of the past two decades is located at a depth between 6 and 9 km, and its compositional fingerprinting derives from mixing processes, likely due to refilling from depth and self-mixing (Métrich et al. 2021). The data set presented in this work offers the opportunity to improve some aspects of the petrogenetic evolution of the deep feeding system. In particular, we suggest that the LP end-member erupted during major explosions derives from the upper portion of the LP reservoir, where magmas become more evolved, due to crystallization of mafic minerals, rather than mixing. During major explosions, this evolved LP end-member commonly erupts together with intermediate magmas residing in the intermediate zones of the feeding system. The intermediate zone is typified by a strongly dynamic petrogenetic evolution dominated by mixing and crystallization processes that transform the LP magma into the HP one. The products from the 19 July 2020 major explosion point to almost equilibrium crystallization in small magma pockets that, before entering into the HP reservoir, remain nearly isolated for a maximum of 11 days, likely in the lower part of the intermediate zone where a highly calcic plagioclase crystallizes. Indeed, this gives a snapshot of the depth in the plumbing system at

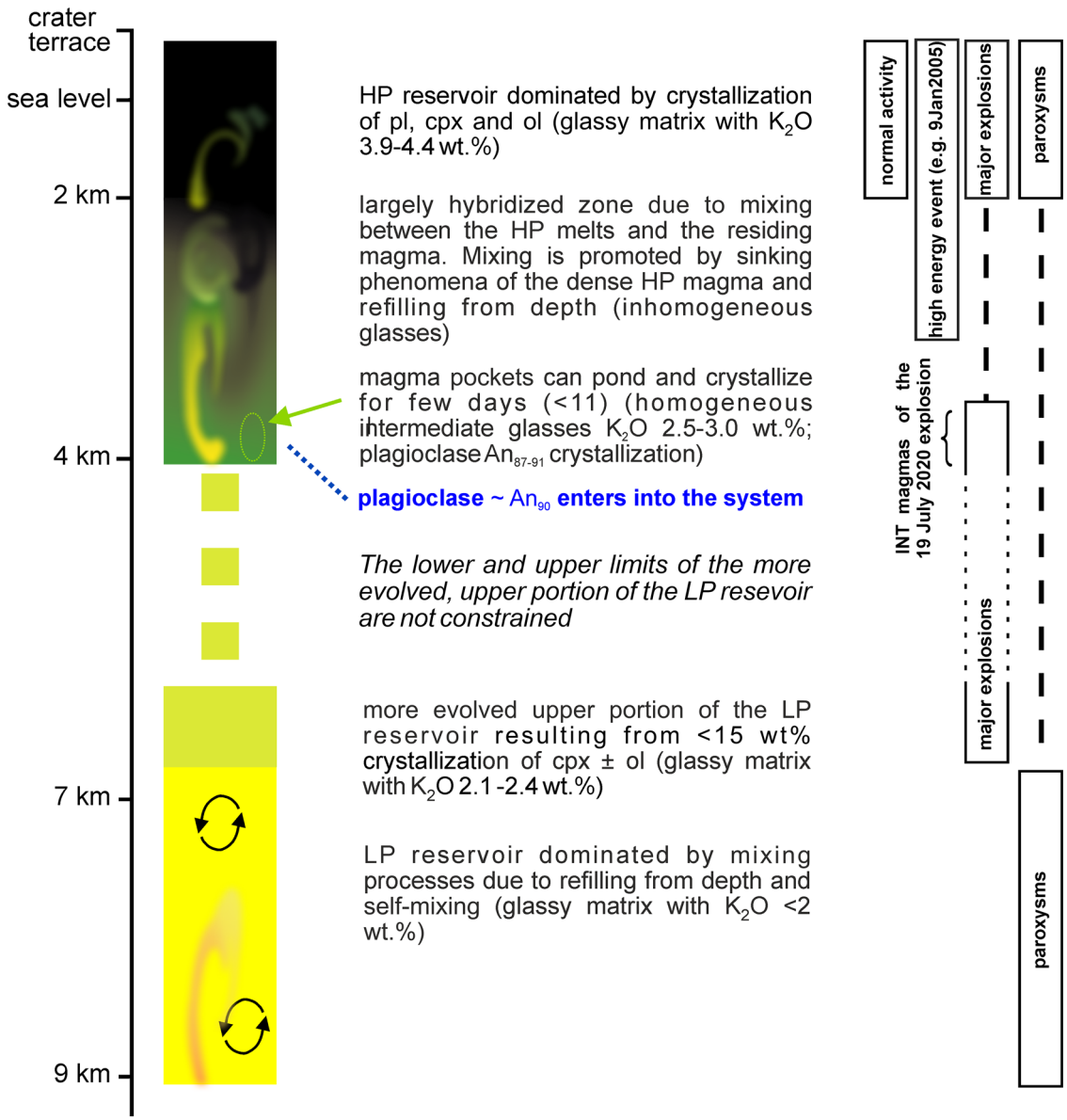

Fig. 10 Schematic representation of the vertically extended magmatic system that feeds the persistent activity at Stromboli volcano. The yellow tones represent the LP magma, the green tones the intermediate magma (INT) and in black the HP magma. The portions of the plumbing system involved in the different types of explosive activity, from normal explosions to paroxysms, are indicated on the right. The large-scale paroxysms of Métrich et al. (2021) are non-represented. Extensive sin-eruptive mixing during major explosions and paroxysms does not allow to discriminate between intermediate melts produced during mixing and those coming from the intermediate zone of the plumbing system (dashed lines). The depth of the different zones of the plumbing system is in part taken from Métrich et al., 2021 (deep LP reservoir), in part are derived from the comparison between the mineralogical characteristics of the products and data from experimental petrology (see text for more explanations)

which the crystallization of the plagioclase begins. In the HK basaltic magma currently emitted at Stromboli, plagioclase crystallization as a result of degassing becomes a dominant process at very shallow levels to produce the HP magmas (plagioclase ~ 66 vol.% of the mineral phases). The largely hybridized zone of the plumbing system is located in the upper part of the intermediate reservoir, where mixing between the HP body and the residing magma, also due to sinking phenomena of the dense HP magma, should be favored. The 9 January 2005 high-energy explosion that erupted intermediate, rather evolved and strongly inhomogeneous melts, with no LP end-member (Landi et al. 2008; Pioli et al. 2014), was likely fed by these strongly hybridized magmas. A relevant conclusion of the above reasoning is that at Stromboli there is a correlation between the magnitude of the explosive events and the depth from which the

magma rises (Fig. 10). According to Schiavi et al. (2010), the different Cr content observed in LP products from paroxysms suggests that the high-Cr melts may have traveled slower within the deep conduits resulting in a longer time of interaction, and thus assimilation, with the deep crystal mush.

Although pumices with intermediate matrix glass were detected among the products erupted between 1998 and 2020, intermediate petrochemical characteristics similar to that observed in the 19 July 2020 vesicular material had never been found. A small quantity of vesicular lapilli with nearly homogeneous, intermediate glasses were erupted about 15 months later, on 6 October 2021. This raises the question of whether the sampling intensification carried out in the last two years (within UNO Project—INGV Departmental Strategic Projects) enabled the collection of products that are present in low quantities, or whether this material was truly absent in the activity of the past decades, thus heralding some changing in the volcano's feeding system. The answer to this delicate question relies on the intensification of product sampling of future eruptions, and more detailed glass analyses of pumice erupted in historical times.

Conclusive remarks

Systematic major- and trace element analyses of the matrix glasses in pumices and scoriae emitted in the past two decades at Stromboli yielded insights into some aspects regarding the chemical evolution and compositional zoning of the plumbing system.

In the following, we listed the main results in which the three chemical groups (LP, Intermediate, and HP magmas) are linked to the plumbing system architecture:

- data highlight small, but significant chemical differences between the products erupted in major explosions and paroxysms, being the glassy matrix in pumices from major explosions slightly more evolved (about < 15 wt.% of cpx + ol crystallization). This points to a vertical chemical zoning of the deep LP reservoir and indicates that major explosions are fed by magmas that rise from the upper portions of the LP system, while the deeper portion of the LP reservoir is only involved during the paroxysms;
- the occurrence of primary magmas with different Cr content is confirmed. Among the studied eruptions, the most energetic paroxysms (5 April 2003 and 3 July 2019) are associated with Cr-poor magmas;
- among the products erupted between 1998 and 2020, intermediate products with a rather homogeneous matrix glass carrying microphenocrysts of plagioclase An_{90} have been sampled for the first time. These samples give a snapshot of a pocket of magma that remains locally isolated few days in a dike-like system, at a depth of 100–50 MPa where the plagioclase crystallization and thus the real transformation from LP to HP magmas begins. With pressure decreasing, volatile loss inducing plagioclase crystallization, magma mixing, and hybridization phenomena become more and more extensive up to the formation of the crystal-rich, shallow HP magma;
- the small compositional differences in the HP matrix glasses are linked to a moderate degree of crystallization. The variability of Cr and Ni contents observed in LP and intermediate magmas is no longer recognizable in the residual matrix glass due to continuous mixing, degassing, and crystallization within the shallow reservoir;
- compositional variations between the products erupted in the different types of explosive activity at Stromboli indicate a relationship between the magnitude of the explosions and the depth of the supply magma. This interpretation, if confirmed by future eruptions, could represent an important step forward to understanding the dynamics of the pre/syn-eruptive magma that drives the volcano's calamitous events, to be compared also with geophysical and geochemical data.

Supplementary Information The online version contains supplementary material available at https://doi.org/10.1007/s00410-022-01962-1.

Acknowledgements This work was supported by the funding provided by MIUR-PRIN 2017, Project "Time scales of solidification in magmas: applications to volcanic eruptions, silicate melts, glasses, glass-ceramics," and INGV–Progetti Strategici Dipartimentali 2019, Project "UNO: UNderstanding the Ordinary to forecast the extraordinary: an integrated approach for studying and interpreting the explosive activity at Stromboli volcano." MP also acknowledges the MIUR-PRIN 2020 (202037YPCZ_001), Project "Dynamics and timescales of volcanic plumbing systems: a multidisciplinary approach to multifaceted problem." The authors are really thankful to the Editor G. Moore, and T. Ubide and two Anonymous Reviewers, whose comments and suggestions improved the early version of the work.

Funding Open access funding provided by Istituto Nazionale di Geofisica e Vulcanologia within the CRUI-CARE Agreement.

References

Aiuppa A, Bitetto M, Delle Donne D, La Monica FP, Tamburello G, Coppola D, Della Schiava M, Innocenti L, Lacanna G, Laiolo M, Massimetti F, Pistolesi M, Silengo MC, Ripepe M (2021) Volcanic CO_2 tracks the incubation period of basaltic paroxysms. Sci Adv 2021:7

Agostini C, Fortunati A, Arzilli F, Landi P, Carroll MR (2013) Kinetics of crystal evolution as a probe to magmatism at Stromboli (Aeolian Archipelago, Italy). Geochim Cosmochim Acta 110:135–151

Andronico D, Corsaro RA, Cristaldi A, Polacci M (2008) Characterizing high energy explosive eruptions at Stromboli volcano using multidisciplinary data: an example for the 9 January 2005 explosion. J Volcanol Geotherm Res 176:541–550

Andronico D, Pistolesi M (2010) The November 2009 paroxysmal explosions at Stromboli. J Volcanol Geotherm Res 196:120–125

Andronico D, Del Bello E, D'Oriano C, Landi P, Pardini F, Scarlato P, de Michieli VM, Taddeucci J, Cristaldi A, Ciancitto F, Pennacchia F, Ricci T, Valentini F (2021) Uncovering the eruptive patterns of the 2019 double paroxysm eruption crisis of Stromboli volcano. Nat Commun. https://doi.org/10.1038/s41467-021-24420-1

Armienti A, Francalanci L, Landi P (2007) Textural effects of steady state behaviour of the Stromboli feeding system. J Volcanol Geotherm Res 160:86–98

Bamber EC, Arzilli F, Polacci M, Hartley ME, Fellowes J, Di Genova D, Chavarrìa D, Samallos JA, Burton MR (2020) Pre- and syn-eruptive conditions of a basaltic Plinian eruption at Masaya Volcano, Nicaragua: The Masaya Triple layer (2.1 ka). J Volcanol Geotherm Res. https://doi.org/10.1016/j.jvolgeores.2019.106761

Barberi F, Rosi M, Sodi A (1993) Volcanic hazard assessment at Stromboli based on review of historical data. Acta Vulcanol 3:173–187

Bertagnini A, Di Roberto A, Pompilio M (2011) Paroxysmal activity at Stromboli: lessons from the past. Bull Volcanol 73:1229–1243

Bertagnini A, Métrich N, Land P, Rosi M (2003) Stromboli an open window on the deep feeding system of a steady state volcano. J Geoph Res. https://doi.org/10.1029/2002JB002146

Bertagnini A, Coltelli M, Landi P, Pompilio M, Rosi M (1999) Violent explosions yield new insights into dynamics of Stromboli volcano. Eos Trans AGU 80:633–636

Bertagnini A, Métrich N, Francalanci L, Landi P, Tommasini S, Conticelli S (2008) Volcanology and magma geochemistry of the present-day activity: constraints on the feeding system. In: Calvari S, Inguaggiato S, Puglisi G, Ripepe M, Rosi M (eds). Learning from Stromboli. American Geophysical Union, Washington, Geophysical Monograph 182. pp 19–38

Conte AM, Perinelli C, Trigila R (2006) Cooling kinetics experiments on different Stromboli lavas: effects on crystal morphologies and phases composition. J Volcanol Geoth Res 155:179–200

D'Oriano C, Bertagnini A, Pompilio M (2011) Ash erupted during normal activity at Stromboli (Aeolian Islands, Italy) raises questions on how the feeding system works. Bull Volcanol 73:471–477

D'Oriano C, Da Pelo S, Podda F, Cioni R (2008) Laser-Ablation Inductively Coupled Plasma Mass Spectrometry (LA-ICP-MS): setting operating conditions and instrumental performance. Per Mineral 77:65–74

Di Carlo I, Pichavant M, Rotolo SG, Scaillet B (2006) Experimental crystallization of high-K arc basalt: the golden pumice, Stromboli volcano (Italy). J Petrol 47:1317–1343

Di Stefano F, Mollo S, Ubide T, Petrone CM, Caulfield J, Scarlato P, Nazzari M, Andronico D, Del Bello E (2020) Mush cannibalism and disruption recorded by clinopyroxene phenocrysts at Stromboli volcano: new insights from recent 2003–2017 activity. Lithos. https://doi.org/10.1016/j.lithos.2020.105440

Ersoy EY (2013) PETROMODELER (Petrological Modeler): a Microsoft® Excel© spreadsheet program for modelling melting, mixing, crystallization and assimilation processes in magmatic systems. Turkish J Earth Sci 22:115–125

Francalanci L, Tommasini S, Conticelli S (2004) The volcanic activity of Stromboli in the 1906–1998 AD period: mineralogical, geochemical and isotope data relevant to the understanding of the plumbing system. J Volcanol Geotherm Res 131:179–211

Francalanci L, Avanzinelli R, Nardini I, Tiepolo M, Davidson LP, Vannucci R (2012) Crystal recycling in the steady-state system of the active Stromboli volcano: a 2.5-ka story inferred from in situ Sr-isotope and trace element data. Contrib Mineral Petrol 163:109–131

Francalanci L, Davies GR, Lustenmhower W, Tommasini S, Mason PRD, Conticelli S (2005) Old crystal re-cycle and multiple magma reservoirs in the plumbing system of the present day activity at Stromboli volcano, South Italy: Sr-isotope in situ microanalyses. J Petrol 46:1997–2021

Harris A, Ripepe M (2007) Temperature and dynamics of degassing at Stromboli. J Geoph Res. https://doi.org/10.1029/2006jb004393

La Felice S, Landi P (2011a) The 2009 paroxysmal explosions at Stromboli (Italy): magma mixing and eruption dynamics. Bull Volcanol 73:1147–1154

La Felice S, Landi P (2011b) A spatter-forming, large-scale paroxysm at Stromboli Volcano (Aeolian Islands, Italy): insight into magma evolution and eruption dynamics. Bull Volcanol 73:1393–1406

Landi P, Marchetti E, La Felice S, Ripepe M, Rosi M (2011) Integrated petrochemical and geophysical data reveals thermal distribution of the feeding conduits at Stromboli volcano, Italy. Geophys Res Lett. https://doi.org/10.1029/2010GL046296

Landi P, Métrich N, Bertagnini A, Rosi M (2004) Dynamics of magma mixing and degassing recorded in plagioclase at Stromboli (Aeolian Archipelago, Italy). Contrib Mineral Petrol 147:213–227

Landi P, Métrich N, Bertagnini A, Rosi M (2008) Recycling and "rehydration" of degassed magma inducing transient dissolution/crystallization events at Stromboli (Italy). J Volcanol Geotherm Res 174:325–336

Landi P, Corsaro RA, Francalanci L, Civetta L, Miraglia L, Pompilio M, Tesoro R (2009) Magma dynamics during the 2007 Stromboli eruption (Aeolian Islands, Italy): mineralogical, geochemical and isotopic data. J Volcanol Geotherm Res 182:255–268

Mercalli G (1907) I vulcani attivi della Terra. Hoepli, Milan, Italy

Métrich N, Bertagnini A, Di Muro A (2010) Conditions of magma storage, degassing and ascent at Stromboli: new insights into the volcano plumbing system with inferences on the eruptive dynamics. J Petrol 51:603–626

Métrich N, Bertagnini A, Pistolesi M (2021) Paroxysms at Stromboli Volcano (Italy): source, genesis and dynamics. Front Earth Sci 9:1–17

Métrich N, Bertagnini A, Landi P, Rosi M (2001) Crystallization driven by decompression and water loss at Stromboli volcano (Aeolian Islands, Italy). J Petrol 42:1471–1490

Métrich N, Bertagnini A, Landi P, Rosi M, Belhadj O (2005) Triggering mechanism at the origin of paroxysms at Stromboli (Aeolian archipelago, Italy): the 5 April 2003 eruption. J Geoph Res. https://doi.org/10.1029/2004GL022257

Paton C, Hellstrom J, Paul B, Woodhead J, Hergt J (2011) Iolite: Freeware for the visualization and processing of mass spectrometric data. J Anal at Spectrom 26:2508–2518

Pearce JGN, Perkins WT, Westgate JA, Gorton MP, Jackson SE, Neal CR, Chenery SP (1997) A compilation of new and published major and trace element data for NIST SRM 610 and NIST SRM 612 glass reference materials. Geostand Newsl 21:115–144

Peccerillo A, Taylor SR (1976) Geochemistry of Eocene calc-alkaline volcanic rocks from the Kastamonu area, Northern Turkey. Contrib Mineral Petrol 58:63–81

Perugini D, Petrelli M, Poli G (2006) Diffusive fractionation of trace elements by chaotic mixing of magmas. Earth Planet Sci Lett 243:669–680

Perugini D, De Campos CP, Dingwell DB, Petrelli M, Poli G (2008) Trace element mobility during magma mixing: Preliminary experimental results. Chem Geol 256:146–157

Petrelli M, Morgavi D, Vetere F, Perugini D (2016a) Elemental imaging and petro-volcanological applications of an improved laser ablation inductively coupled quadrupole plasma mass spectrometry. Per Mineral 85:25–39

Petrelli M, Laeger K, Perugini D (2016b) High spatial resolution trace element determination of geological samples by laser ablation quadrupole plasma mass spectrometry: implications for glass analysis in volcanic products. Geosci J 20:851–863

Pichavant M, Di Carlo I, Le Gac Y, Rotolo SG, Scaillet B (2009) Experimental constraints on the deep magma feeding system at Stromboli volcano, Italy. J Petrol 50:601–624

Pichavant M, Di Carlo I, Pompilio M, Le Gall N (2022) Timescales and mechanisms of paroxysm initiation at Stromboli volcano, Aeolian Islands, Italy. Bull Volcanol 84:36

Pichavant M, Pompilio M, D'Oriano C, Di Carlo I (2011) Petrography, mineralogy and geochemistry of a primitive pumice from Stromboli: implications for the deep feeding system. Eur J Mineral 23:499–517

Pioli L, Pistolesi M, Rosi M (2014) Transient explosions at open-vent volcanoes: the case of Stromboli (Italy). Geology 133:429. https://doi.org/10.1130/G35844.1

Pompilio M, Bertagnini A, Métrich N (2012) Geochemical heterogeneities and dynamics of magmas within the plumbing system of a persistently active volcano: evidence from Stromboli. Bull Volcanol 74:881–894

Rosi M, Pistolesi M, Bertagnini A, Landi P, Pompilio M, Di Roberto A (2013) Stromboli volcano, Aeolian Islands (Italy): present eruptive activity and hazards. Geol Soc Mem 37:473–490

Schiavi F, Kobayashi K, Moriguti T, Nakamura E, Pompilio M, Tiepolo M, Vannucci R (2010) Degassing, crystallization and eruption dynamics at Stromboli: trace element and lithium isotopic evidence from 2003 ashes. Contrib Mineral Petrol 159:541–561

Tibaldi A (2001) Multiple sector collapses at Stromboli volcano, Italy: how they work. Bull Volcanol 63:112–125

Ubide T, Caulfield J, Brandt C, Bussweiler Y, Mollo S, Di Stefano F, Nazzari M, Scarlato P (2019) Deep magma storage revealed by multi-method elemental mapping of clinopyroxene megacrysts at stromboli volcano. Front Earth Sci. https://doi.org/10.3389/feart.2019.00239

Wilson SA (1997) The collection, preparation, and testing of USGS reference material BCR-2, Columbia River, Basalt. U.S. Geological Survey Open-File Report vol. 98